energies

MDPI

Article

Integrated Approach to Reservoir Simulations for Evaluating Pilot CO_2 Injection in a Depleted Naturally Fractured Oil Field On-Shore Europe

Milan Pagáč [1,*], Vladimír Opletal [1], Anton Shchipanov [2], Anders Nermoen [2], Roman Berenblyum [2], Ingebret Fjelde [2] and Jiří Rez [3]

[1] MND—Moravské Naftové Doly, Úprkova 807/6, 695 01 Hodonín, Czech Republic; opletal@mnd.cz
[2] NORCE—Norwegian Research Centre, Nygårdsgaten 112, 5008 Bergen, Norway; ansh@norceresearch.no (A.S.); aner@norceresearch.no (A.N.); robe@norceresearch.no (R.B.); infj@norceresearch.no (I.F.)
[3] CGS—Czech Geological Survey, Leitnerova 22, 658 69 Brno, Czech Republic; jiri.rez@geology.cz
* Correspondence: pagac@mnd.cz

Abstract: Carbon dioxide capture and storage (CCS) is a necessary requirement for high-emitting CO_2 industries to significantly reduce volumes of greenhouse gases released into the atmosphere and mitigate climate change. Geological CO_2 storage into depleted oil and gas fields is the fastest and most accessible option for CCS deployment allowing for re-purposing existing infrastructures and utilizing significant knowledge about the subsurface acquired during field production operations. The location of such depleted fields in the neighborhoods of high-emitting CO_2 industries is an additional advantage of matured on-shore European fields. Considering these advantages, oil and gas operators are now evaluating different possibilities for CO_2 sequestration projects for the fields approaching end of production. This article describes an integrated approach to reservoir simulations focused on evaluating a CO_2 injection pilot at one of these matured fields operated by MND and located in the Czech Republic. The CO_2 injection site in focus is a naturally fractured carbonate reservoir. This oil-bearing formation has a gas cap and connection to a limited aquifer and was produced mainly by pressure depletion with limited pressure support from water injection. The article summarizes the results of the efforts made by the multi-disciplinary team. An integrated approach was developed starting from geological modeling of a naturally fractured reservoir, integrating the results of laboratory studies and their interpretations (geomechanics and geochemistry), dynamic field data analysis (pressure transient analysis, including time-lapse) and history matching reservoir model enabling simulation of the pilot CO_2 injection. The laboratory studies and field data analysis provided descriptions of stress-sensitive fracture properties and safe injection envelope preventing induced fracturing. The impact of potential salt precipitation in the near wellbore area was also included. These effects are considered in the context of a pilot CO_2 injection and addressed in the reservoir simulations of injection scenarios. Single-porosity and permeability reservoir simulations with a dominating fracture flow and black-oil formulation with CO_2 simulated as a solvent were performed in this study. The arguments for the choice of the simulation approach for the site in focus are shortly discussed. The reservoir simulations indicated a larger site injection capacity than that required for the pilot injection, and gravity-driven CO_2 migration pathway towards the gas cap in the reservoir. The application of the approach to the site in focus also revealed large uncertainties, related to fracture description and geomechanical evaluations, resulting in an uncertain safe injection envelope. These uncertainties should be addressed in further studies in preparation for the pilot. The article concludes with an overview of the outcomes of the integrated approach and its application to the field in focus, including a discussion of the issues and uncertainties revealed.

Keywords: carbon capture and storage; reservoir simulation; integrated approach; naturally fractured carbonate reservoir; safe injection envelope; pilot CO_2 injection

Citation: Pagáč, M.; Opletal, V.; Shchipanov, A.; Nermoen, A.; Berenblyum, R.; Fjelde, I.; Rez, J. Integrated Approach to Reservoir Simulations for Evaluating Pilot CO_2 Injection in a Depleted Naturally Fractured Oil Field On-Shore Europe. *Energies* **2024**, *17*, 2659. https://doi.org/10.3390/en17112659

Academic Editor: Krzysztof Skrzypkowski

Received: 26 April 2024
Revised: 22 May 2024
Accepted: 24 May 2024
Published: 30 May 2024

1. Introduction

The characterization, modeling, and simulation of flow in underground reservoirs are generally challenging tasks, while they become more complicated when dealing with naturally fractured carbonates. Well logging and laboratory measurements on core plugs are commonly utilized for characterizing both sandstone and carbonate reservoirs, where special measurements and analyses, like borehole imaging, large-scale core experiments, well testing, and permanent well monitoring, become crucial when dealing with fractured carbonate reservoirs. The fractured reservoirs were comprehensively studied in the context of hydrocarbon production, and specific approaches for reservoir characterization, modeling, and flow simulation for such reservoirs have been developed and applied in the industry for decades [1–6].

When considering geological CO_2 storage in subsurface reservoirs, including depleted oil fields, the evaluation of geochemical [7] and geomechanical [8] effects becomes crucial since the reservoirs' rocks are exposed to new fluid (CO_2) and conditions (pressure and temperature) usually different to previous operational conditions. The hydraulic properties of naturally fractured reservoirs may be sensitive to pressure changes, since these cause effective stress changes influencing fracture aperture [9] with many observations for fractured reservoirs from laboratory experiments [10] and field data [11], and [12]. There are examples of large-scale projects of CO_2 storage in naturally fractured carbonates, where the In Salah storage project is very well documented in the literature [13–15]. According to the literature, the following specific features of CO_2 injection in the fractured reservoir may be highlighted: (1) dominating fracture flow for CO_2 injection; (2) potential uplift of cap rocks due to reservoir pressure build-up; and (3) increase in the hydraulic properties of fracture rocks.

The potential of CO_2 storage in a depleted oil field in the Czech Republic was previously studied for a sandstone reservoir [16] and is extended to a naturally fractured reservoir in the current study within the CO_2-SPICER project [17]. The project mainly focuses on a preparatory work for the pilot itself and developing a roadmap for potential CCS projects in the region, but not concentrating on technical evaluations of long-term large-scale CO_2 storage. Overall, the project aimed at evaluating and demonstrating the CCS technology to local, national, and regional stakeholders, including regulators and competent authorities. Here, obtaining practical experience with a real site assessment, preparation, design of facilities, and CO_2 handling necessary for a pilot CO_2 injection is crucial for paving the way for the deployment of this new technology having large potential for mitigating the climate change observed these days. Another objective of the project was to identify knowledge gaps and additional studies needed to fill these gaps prior to the pilot. Choosing a mature petroleum field for the CO_2 pilot has many advantages, including (1) the ability to utilize existing wells, (2) infrastructure (well sites and roads), (3) surface facilities, and (4) to benefit from available subsurface knowledge already gained during the development of the field. Therefore, using an oil field at the final production phase seems to be a logical choice in comparison with a deep saline aquifer, where limited data, knowledge, and facilities are usually available. As an additional option, we could mention that the remaining gas volume in the gas cap of the field in focus may be considered as a potential source of "blue hydrogen" production, where by-product CO_2 may be stored in the same reservoir, from where the gas is produced.

CO_2-EOR should also be mentioned as one of the potential measures to improve overall project economy, as shown in the evaluations performed in previous projects [16,18]. However, CO_2-EOR was not evaluated in this work due to the following factors: the lack of a regulatory approach in transitioning CO_2-EOR to CO_2 storage and considerable additional experimental and simulation work required to properly evaluate and optimize CO_2-EOR for both recovery and storage amounts.

This paper focuses on describing an integrated approach that was employed to improve reservoir and fluid flow descriptions in the reservoir simulations to be capable of evaluating a pilot CO_2 injection for the chosen site. Injecting CO_2 has specific features,

which are not covered when studying a producing petroleum reservoir. This may include additional studies on geochemistry effects, such as CO_2-rock interactions and salt precipitation; on geomechanics, to assess the CO_2 impact of geomechanical parameters and impact of pressure build-up on reservoir and cap-rock deformations; and other studies depending on the scope and scale of the CO_2 injection project. Since the pilot injection is the focus of this study, we limited our scope by studying specific effects crucial for the pilot's performance, such as evaluating the safe injection envelope allowing natural fracture opening but preventing induced fracturing and the potential impact of geochemistry effects on well injectivity related to salt precipitation. Fracture characterization was also focused on since natural fractures govern reservoir flow capacity and the pilot performance as well.

The paper is structured in the following way: Section 2 outlines the integrated approach used for preparing and carrying out reservoir simulations, including history matching the reservoir flow model and simulation of the pilot CO_2 injection. Section 3 describes the application of this integrated approach to the site in focus, with the results contributing to assembling the reservoir model and matching it to the hydrocarbon production history to ensure a proper reservoir description. The section terminates with the simulation results for the CO_2 injection pilot. Section 4 discusses the applicability and limitations of our analysis in combination with the knowledge gaps and additional studies to fill in these gaps, where the study conclusions are presented in Section 5.

2. An Integrated Approach to Reservoir Simulations of the Pilot CO_2 Injection

In this section, an integrated approach for reservoir simulations is introduced combining (1) capturing the main features of fluid flow in the fractured carbonate reservoir in focus from (1.1) geological modeling through (1.2) dynamic data analysis (DDA) to (1.3) history matching at the first stage toward (2) simulating the pilot CO_2 injection at the second stage. Figure 1 represents the schematics of the integrated approach combining these two stages. Different sub-components of the integrated approach provide contributions at different or both stages, including 'Petrophysics', 'Seismic', 'Well logs', 'pressure–volume–temperature analysis (PVT)', 'special core analysis (SCAL)' (the first stage), 'Compositional effects' and 'Geochemistry' (the second stage), and 'Geomechanics' (both stages).

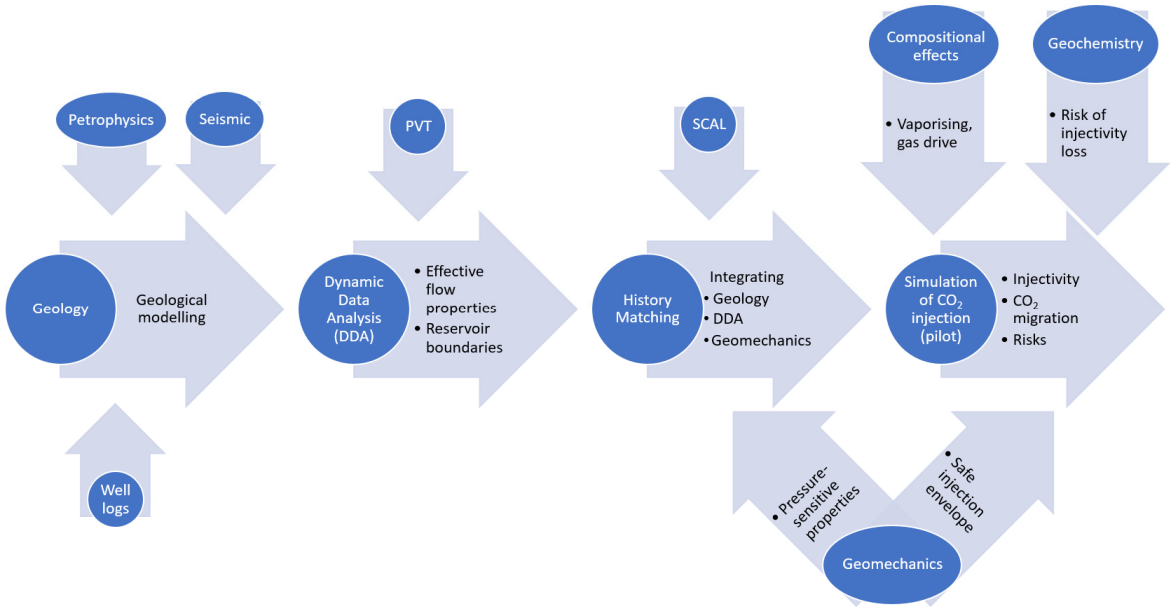

Figure 1. Workflow of the integrated approach.

The first stage includes conventional steps of assembling and matching a three-dimensional (3D) model of a fractured reservoir, as is commonly performed in the oil and gas industry. Here, the geological model integrates petrophysical, seismic, and well

logging data [17]. Laboratory experiments with the reservoir fluids resulted in estimating their PVT properties further employed in the dynamic data analysis carried out to estimate the effective hydraulic properties of the fractured reservoir and reservoir boundaries, i.e., the extent of the reservoir storage complex and how it is hydraulically connected to an aquifer. An understanding of the boundary conditions and the reservoir volume may be gained from the pressure dynamics during production, which will follow CO_2 injection. Integrating the results of the SCAL representing the multiphase flow mechanics dictated by wettability, capillary effects, and, finally, relative permeabilities helps to describe and match the multiphase flow in the 3D reservoir model to the observed oil, gas, and water production and pressure dynamic history. The results of the geomechanical experiments contribute to the reservoir simulations with the pressure-dependent functions of reservoir porosity and permeability.

This integrated approach enabled the team to develop a sufficient understanding of the reservoir complex to make credible estimates of future CO_2 injections. The CO_2 simulations include additional information on the compositional effects of the fluid phases as well as geochemical effects (like potential salt precipitation). Geomechanics contributes at this stage with a safe injection envelope that enables the operator to develop a low-risk injection scenario. This envelope describes pressures and temperatures, where the opening of existing fractures is expected, followed by the possibility of tensile (induced fracturing) and shear failures (e.g., fault reactivation). These injection scenarios, i.e., how much CO_2 the reservoir can take and at what rate within the injection pressure limitations, are fundamental to the whole value chain evaluation. For example, these scenarios help to evaluate the capacity of transportation systems to be developed and to assess the capture projects that should be developed in the region to provide sufficient CO_2 volumes for such scenarios.

The next sections of this paper describe how this integrated approach has been applied to the reservoir in focus, with the most attention paid to the components marked by large arrows in Figure 1 in order to provide a robust description of the fractured reservoir (such as DDA, history match, and geomechanics) and carry out reliable CO_2 injection simulations (such as compositional effects, geochemistry, and geomechanics). The conventional components indicated by small arrows (petrophysics, seismic, well logs, PVT, and SCAL) are granted less attention in the paper to limit its size.

3. Application of the Integrated Approach to a Depleted Fractured Oil Field

The integrated approach illustrated in Figure 1 has been tested via application to the field in focus, where a multi-disciplinary team was working combining different approaches and studies, including laboratory experiments and their interpretations, field data analysis, and, finally, 3D reservoir modeling and simulations. Accounting for the study objectives, human and financial resources available and the study duration, the one-model-realization approach to geological modeling and reservoir simulations has been chosen in contrast to the ensemble-based approach with multiple model realizations currently used in the industry. Although the one-realization approach does not allow for accounting and propagating throughout the simulation forecast the uncertainties resulting from well and field data interpretations and modeling, obviously present in studying such complicated reservoir settings, it enables the time-effective testing of the integrated approach in the context of preparation for the pilot CO_2 injection. The results of such testing may be useful beyond the evaluation of the geological setting in focus, since a combination of different components of the approach is of interest and is one of the major objectives of this study. The following sections provide a short description of the study following the workflow in Figure 1.

3.1. Geological Modeling as the Conventional Basis for Reservoir Simulations

The field in focus is located 30 km South-East of Brno in Southern Moravia in the South-Eastern part of the Czech Republic. It was discovered in 2001 at depths ranging from

1565 to 1872 m. The field had four vertical and four horizontal production wells. The field had a large gas cap on top of the oil zone with a limited saline aquifer connected. Most of oil and a significant volume of initial gas reserves were produced by 2023, and the field is approaching the end phase of hydrocarbon production.

The producing reservoir is situated in a complex geological setting, where the basement is formed by Precambrian-age crystalline rocks, directly overlain by the Paleozoic depositional system of Cambrian to Carboniferous ages. The reservoir is formed mostly by Vranovice limestone and Nikolčice formation with an overall thickness of up to 300 m. Both Mikulov Marl and the Paleogene pelites form the main sealing (Figure 2).

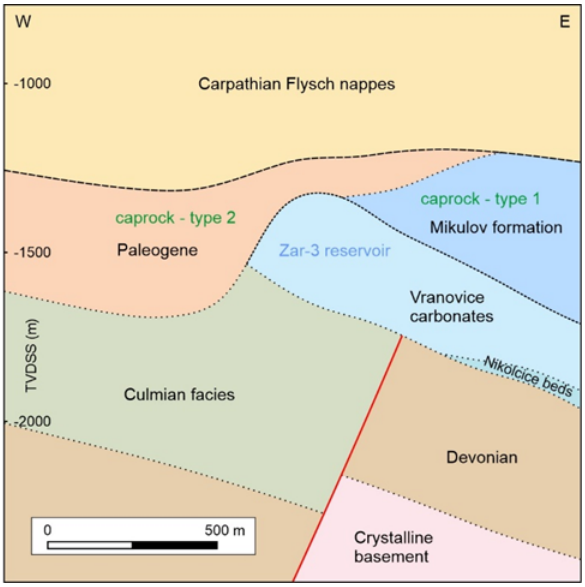

Figure 2. Geological cross-section of the storage complex [17].

The Vranovice formation (depicted in Figure 3) is formed by naturally fractured carbonate rocks. The petrology and geochemistry of the storage complex were studied and described in [19]. The gas cap initially reached a thickness up to 150 m, and the original oil zone was approximately 105 m thick. Gas–oil contact and oil–water contact (GOC and OWC) at depths of 1490 and 1595 m, respectively, were estimated based on well logging data and drill-stem tests. Both contacts are periodically updated during production by logging in the observation well.

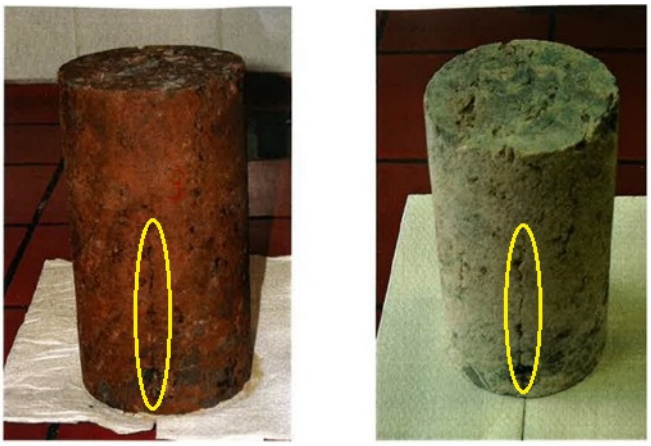

Figure 3. Images of whole diameter core from the Vranovice carbonate formation for well ZA4A; depth: 1781–1781.3 m. The (**left**) image displays a core sample before and (**right**) image after cleaning and drying. Fracture located in the core is marked in yellow.

The 3D structural model served as the basis for geological modeling and further reservoir simulations. The 3D geological model, including its lithostratigraphic units, is based on seismic interpretation and fluid constituency data from wells test results, and was assembled using Petrel software (version 2020.4). The geological modeling and property distributions were carried out based on interpretations of the well logging data, including gamma ray, spontaneous potential, resistivity, neutron, density, and sonic logs. These interpretations were complemented by caliper logs and NMR (nuclear magnetic resonance) data when available. The 3D geological model assembled covered an area larger than the reservoir itself, including an aquifer zone and the cap rocks, accounting for the potential use of the model in future studies. The reservoir part of the geological model is shown in Figure 4, also describing the fluid constituency and the well trajectories.

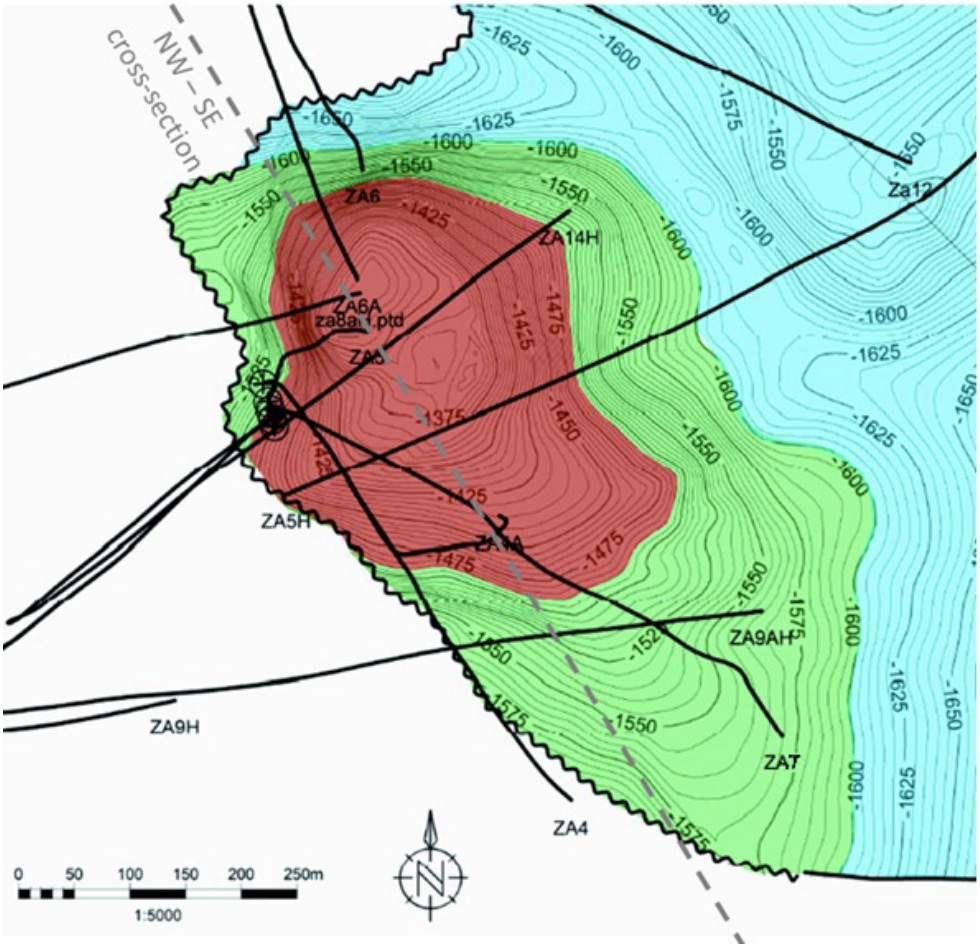

Figure 4. Top-view depth map of the field with gas (red), oil (green), and water (blue)-saturated areas with well trajectories. The NW–SE (North-West and South-East) cross-section is further used in reservoir characterization studies.

Several techniques were applied in combination to distribute the matrix porosity in the reservoir, including density-neutron cross-plots and density, neutron, and sonic logs, while the resulting porosity distribution was also corrected for clay mineral presence. Figure 5 illustrates the porosity map resulting from the geological model.

The initial water saturation was distributed using the resistivity of the formation water, effective porosity, cementing factor, and Archie's constant. Apart from the routine core analysis on small core plugs, a special core analysis was also carried out on the well-diameter core samples based on core availability. The matrix permeability was distributed using the correlations with effective porosity and water saturation. Well test data and temperature logging were used to evaluate the temperature profile over depth. Finally,

the Gaussian sequential simulation was employed to distribute the parameters described above within the reservoir volume.

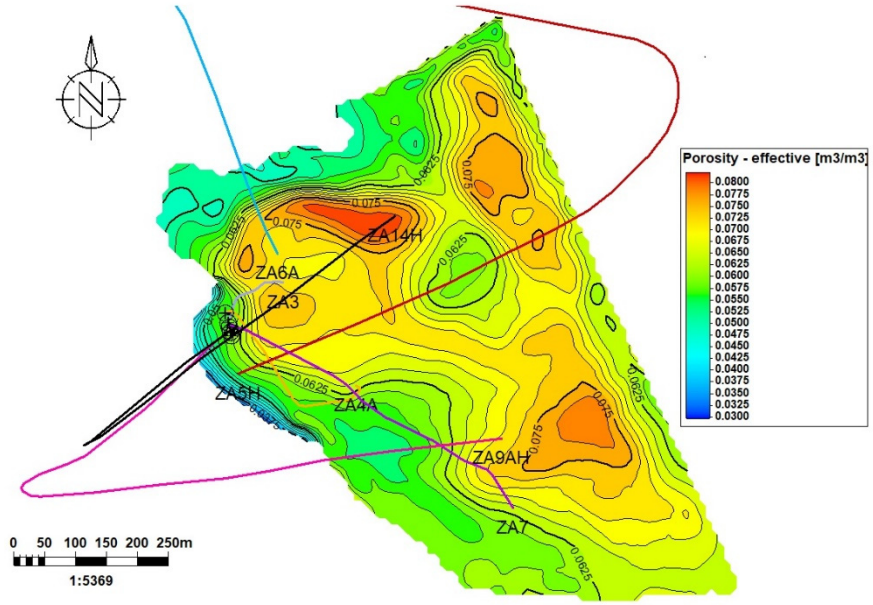

Figure 5. Porosity map resulting from the geological model.

The reservoir in focus consists of naturally fractured carbonate rocks calling for special attention and specific methods for fracture assessment, characterization, and modeling. The natural fracture networks were characterized using formation micro scanner (FMS) logs obtained for seven wells penetrating the field. Examples of the fracture analysis and characterization using FMS data in the ZA3 well are illustrated in Figures 6 and 7. Unfortunately, these FMS data cannot be calibrated by core data since no oriented core samples are available.

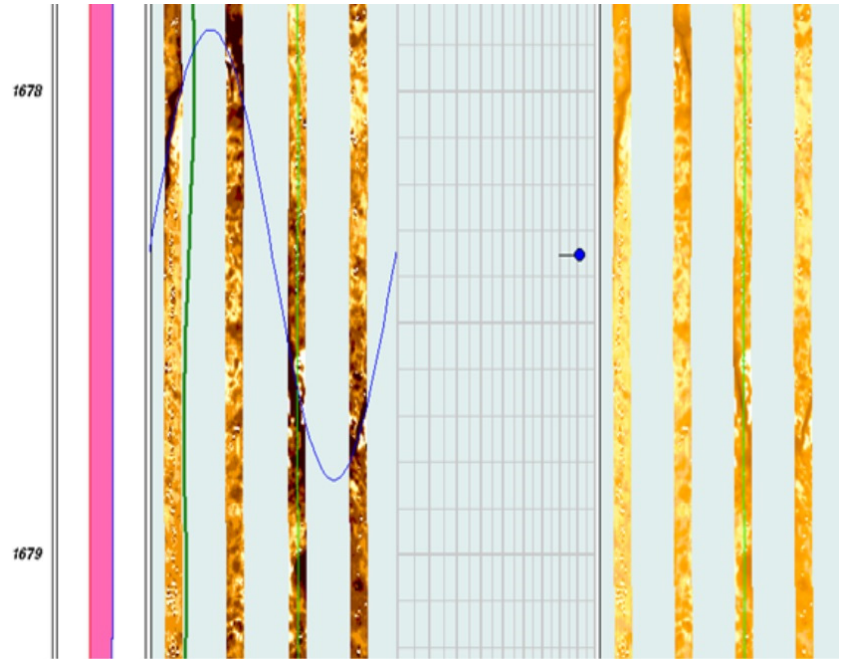

Figure 6. A conductive fracture (displayed in blue) dipping 80 degrees toward 270° West from the FMS logging in well ZA3.

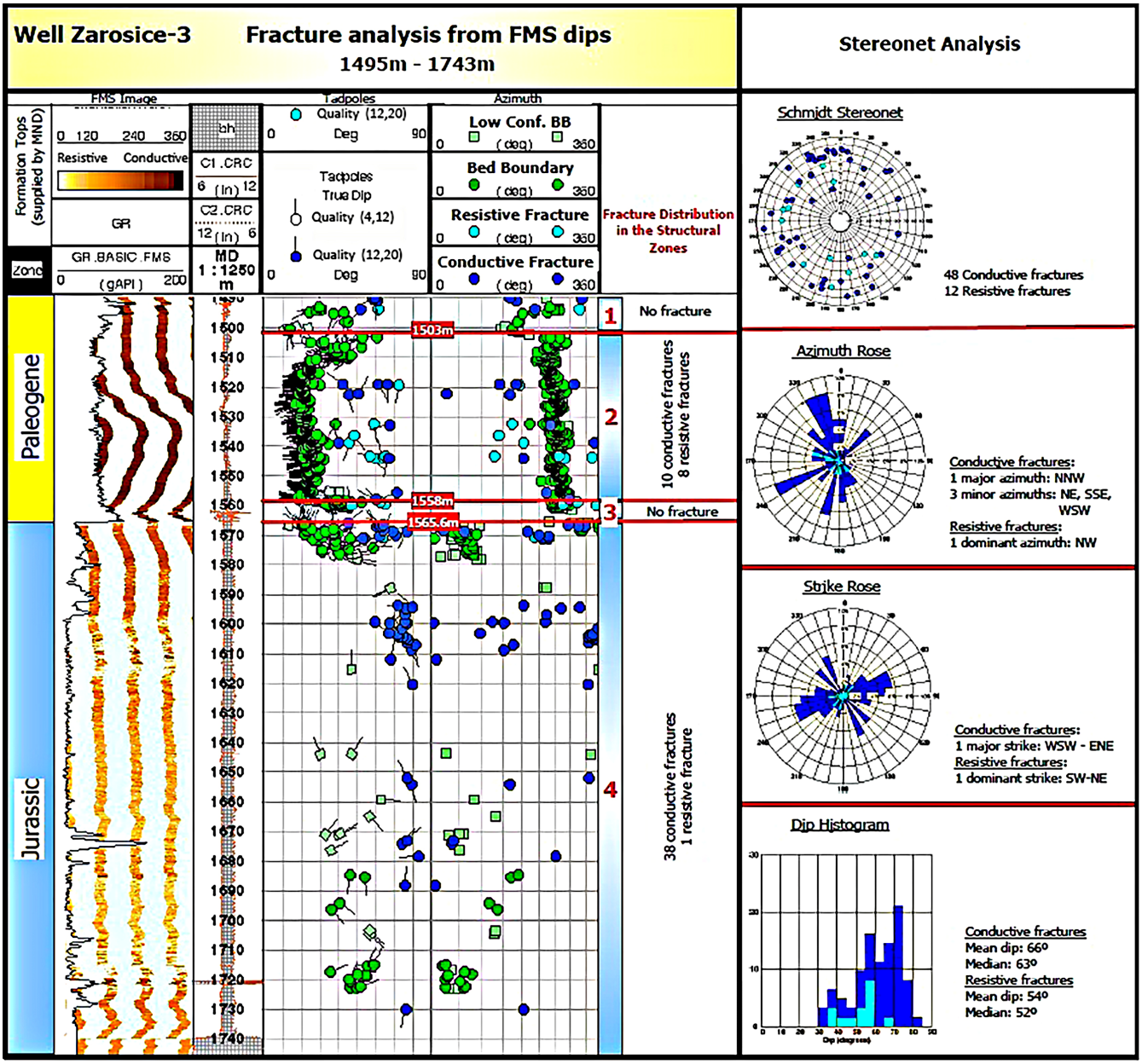

Figure 7. Fracture analysis based on FMS data for ZA3 well.

The usual method for fracture modeling at the reservoir scale is to distribute the fracture properties obtained for particular wells in the whole reservoir volume using the statistical characteristics of fracture sets. However, due to the large size of the geological model, this was not a viable option, and a simpler process was used where the densities of each fracture set (i.e., number of fractures per meter, also termed as 'intensities') were distributed throughout the geological model using their statistical characteristics (mean orientation and dispersion). A map of the fracture intensity is displayed in Figure 8. The resulting densities were then used to calibrate the reservoir properties yielded from the well log analysis.

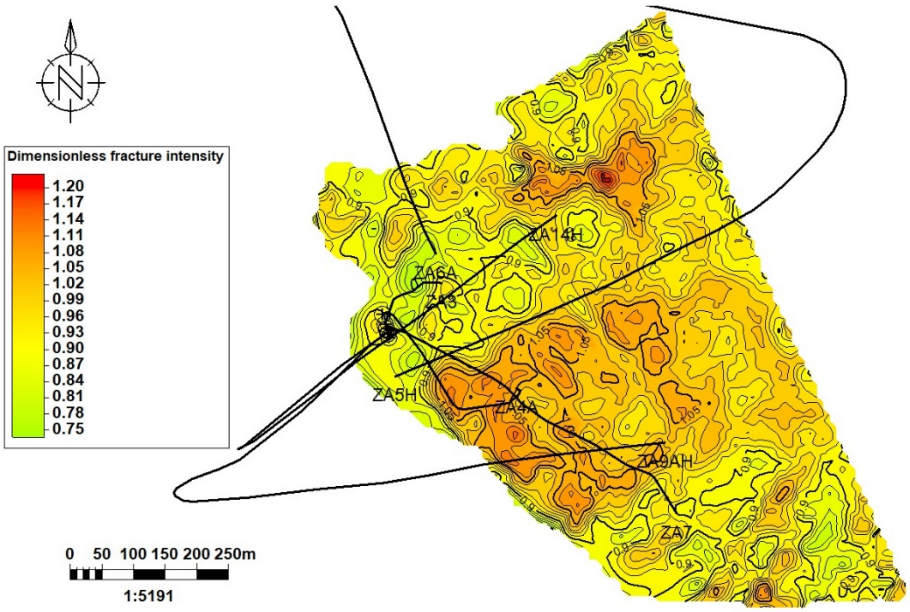

Figure 8. Fracture intensity map resulting from FMS-based fracture analysis and modeling.

3.2. Dynamic Data Analysis

Based on the laboratory investigation of fluid properties, the oil was identified as a medium-heavy one with a specific gravity of 910 kg/m^3 and viscosity of 3.7 cP at the initial reservoir condition. The gas is mainly methane (92%) with 4.8% other hydrocarbon gases and 3.2% nitrogen and CO_2. The original static reservoir pressure was around the hydrostatic pressure value of 180 bars, and the reservoir temperature was 52 °C.

The 20-year field production history is represented by different dynamic datasets, including well tests carried out mainly at the beginning of the production phase and periods of well monitoring with permanent downhole gauges installed. These data were interpreted using a combination of pressure transient analysis (PTA), including time-lapse PTA [20] and history matching with fit-for-purpose reservoir models using Saphir software (version 5.30).

The main objectives of this analysis were to:

- Estimate the reservoir flow capacity (permeability–thickness product, *kh*) and well performance, including skin effects and effective length for horizontal wells.
- Characterize the reservoir boundaries with mapping estimated reservoir properties (such as *kh*) to improve the reservoir description in the reservoir simulations.
- Evaluate the impact of fractures on flow capacity (like dual-porosity and permeability effects) and fracture dynamics (like the pressure sensitivity of reservoir permeability).

Many well tests, including shut-ins at the wellhead or downhole (using a downhole shut-in tool), have been carried, mainly in the initial phase of production. In addition, some production wells were monitored with permanent downhole gauges (PDGs) resulting in long-term pressure measurements during multiple flowing and shut-in periods. These periods provided groups of pressure transients, which may be analyzed using time-lapse PTA methods [20].

The most representative dataset is available for the horizontal producer, ZA-5H, drilled in the central part of the field (Figure 9), used in this paper to illustrate the time-lapse PTA application and its capabilities. Figure 9 displays the PDG data at a 2484 m measured depth (MD) (at the bottom part of the oil zone) for a 2-year history since the beginning of well production, including a few flowing (production) and shut-in (pressure build-up) periods. During these two years, the well was producing above the bubble-point pressure with a minor water cut after a half a year of pure oil production. Two shut-in periods with pressure

build-up (BU1 and 2) and one following production (PROD3) period were analyzed using Saphir software to estimate well and reservoir parameters and reservoir boundaries.

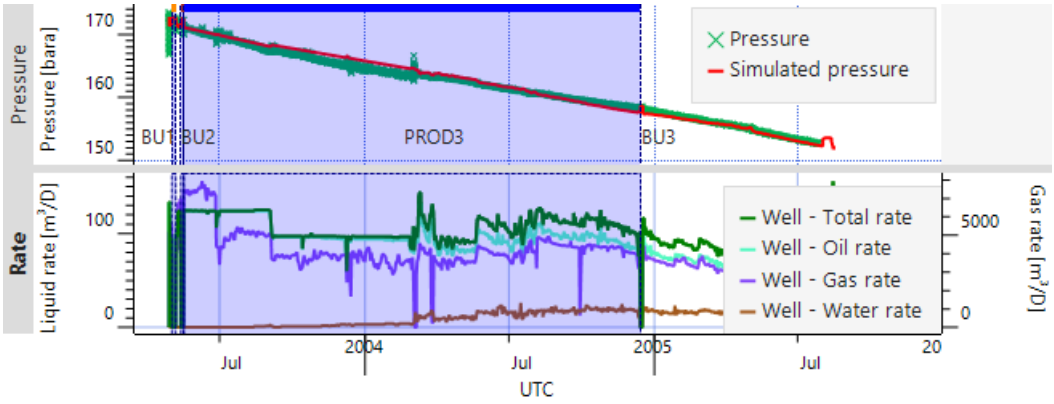

Figure 9. Three sequential shut-in periods (build-ups: BU1, 2, and 3) and one flowing period (production: PROD3). Solid red line for pressure is the result of a simulation with the PTA model.

The production and build-up responses represented in the log–log scale in Figure 10 clearly demonstrate a closed reservoir signature with no-flow boundaries. A fit-for-purpose analytical reservoir model was then used to estimate the reservoir flow capacity, i.e. product of permeability and thickness (*kh*), by using a stabilized pressure derivative level between 1 and 10 hours (h). This model reproduced the closed reservoir response recognized by an increasing derivative during production and decreasing derivative in the build-up periods at late times (i.e., after 10 h).

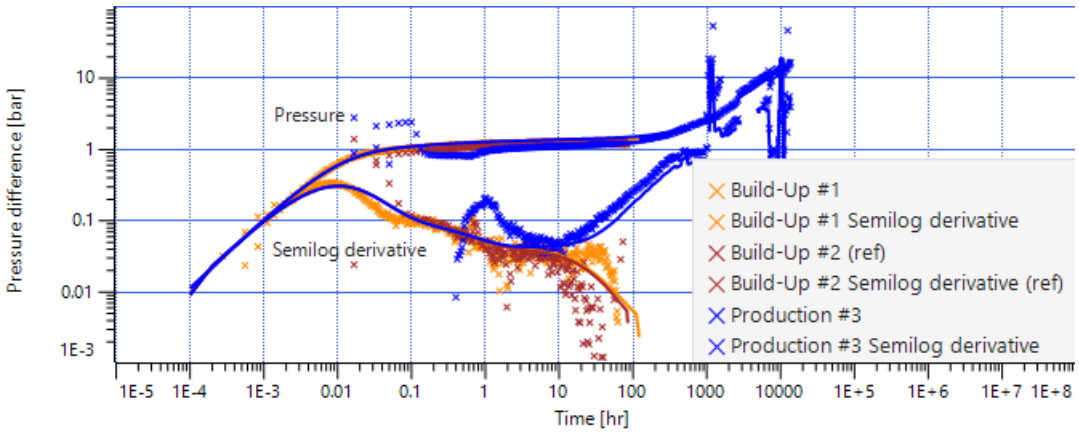

Figure 10. Pressure transient responses in the log–log scale for the build-up and production periods from Figure 9. Solid lines with corresponding colors are simulation results for the PTA model.

A similar PTA interpretation was carried out for well test and pressure monitoring data for other wells (ZA-3, ZA-4A, ZA-9AH, and ZA-7). Pressure build-ups were interpreted for most of the well datasets listed above, where single or repeated build-ups were available. The results of the reservoir characterization based on the dynamic data analysis may be illustrated with the reservoir flow capacity (Figure 11) plotted versus an NW-SE cartesian axis crossing the wells ZA-3 and 4A (as shown in Figure 4).

Among the objectives of dynamic data analysis, one was to evaluate how fractures impacted flow capacity, including possible dual-porosity and permeability effects [4,21]. Moreover, understanding the dynamic fracture behavior and pressure sensitivity of overall reservoir permeability [11] is the key to develop a representative reservoir model that can also be employed for CO_2 injection forecasts.

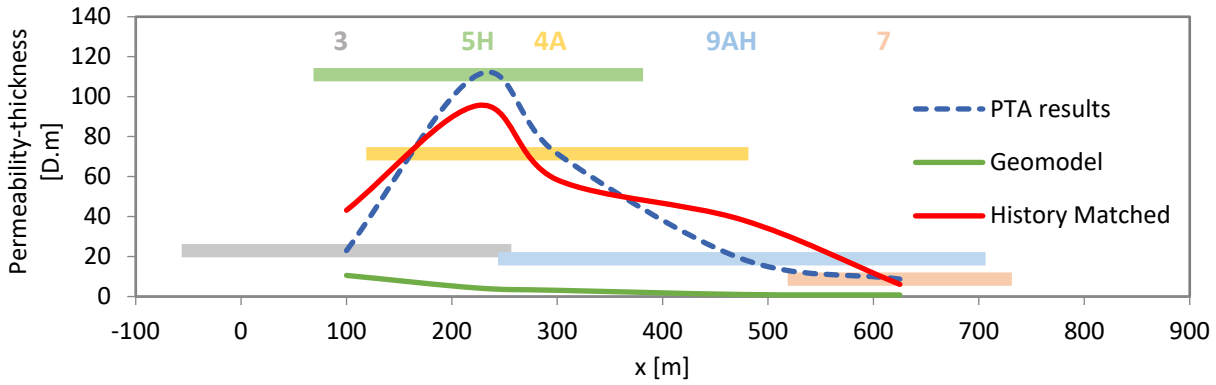

Figure 11. Reservoir flow capacity (*kh*) estimated from the analysis of dynamic data obtained for different production and injection wells (ZA-3, ZA-5H, ZA-4A, ZA-9AH, and ZA-7). The x-axis corresponds to the NW-SE cross-section, as shown in Figure 4.

The dual-porosity and permeability effects are usually governed by high-porosity and permeability contrasts. While matrix porosity may dominate fracture volumes, fracture permeability may dictate the overall flow capacity. This leads to fluid exchange between the matrix and fractures that is reflected in the specific 'saddle-like' signature in the pressure derivative [4,21]. The derivatives for the pressure responses analyzed were quite noisy (Figure 12), so identifying such 'saddle-like' signatures confidently was difficult. A similar noise level was observed in most of the responses that have been analyzed. However, some indication of the signature may be observed for the pressure build-up derivatives in Figure 12 (in the period in the range of 1–3 h) for the well in focus (ZA-5H). A meaningful interpretation with the dual-porosity model was difficult in this case due to the non-representative ratio of parameters to be applied to achieve a derivative match. This signature may also indicate a highly permeable (e.g., intensively fractured) area at some distance from the well. Similar indications of the signature were not found for the other well responses analyzed (keeping in mind the impact of the noise mentioned above), although further work in this direction may be useful for improving the reservoir description.

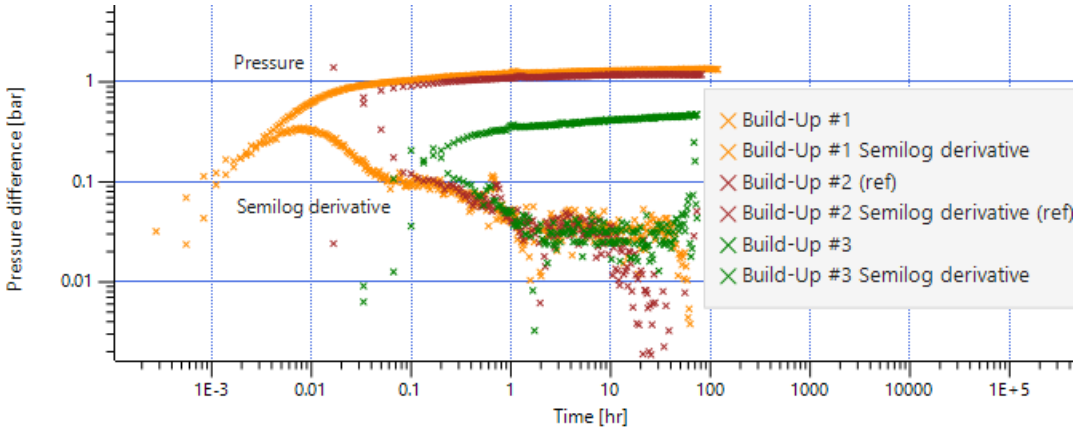

Figure 12. Pressure transient responses in the log–log scale for the build-up and production periods from Figure 9.

The pressure sensitivity of the overall reservoir permeability was observed for many fractured reservoirs, for example [11]. The dynamic field data available were analyzed to find indications of permeability variations caused by pressure changes. However, limited data were available for such a study for this reservoir as tests on the same well were taken only at the beginning of the production for all wells, while permanent monitoring data covered relatively small pressure ranges. As an example, the three build-ups (Figure 12)

may be compared in a time-lapse mode [20] to detect permeability changes, when the characteristic shift (up and down) of pressure derivatives may be observed. The comparison of build-ups 1 and 2 at a reservoir pressure of around 172 bar with build-up 3 at a pressure of around 158 bar is complicated by a high noise level (especially for BU3), making revealing permeability changes difficult. At the same time, the pressure range (158 to 172 bar) may be too small to govern significant permeability changes. As a result, it is difficult to judge the pressure sensitivity of the fractured reservoir considering the data available, and additional surveys (like well tests at different reservoir pressures) are needed to clarify this issue. A step-rate test [12] may be a good candidate for the additional survey, where well performance and permeability changes may be identified. The results of the geomechanical experiments described in the next section, which became available after this dynamic data analysis, show that the opening of natural fractures may happen at a pressure of around 220 bar, which is above the initial reservoir pressure (about 180 bar). This supports the observations made from the dynamic data analysis, although for a quite narrow pressure range.

The following summarizes the dynamic data analysis:

- Reservoir flow capacity (permeability times reservoir thickness, *kh*) and well performance (skin, effective well length for horizontal wells) were estimated for five wells.
- Reservoir characterization with *kh* mapping was carried out based on the results obtained for individual wells providing input for reservoir simulations.
- Dual-porosity, permeability, and fracture dynamics (pressure sensitivity) effects were not univocally observed from the interpretations of the field data available.
- Additional well surveys, such as step-rate tests, may be designed using the fit-for-purpose reservoir models employed in PTA to evaluate injection performance.

3.3. Geomechanics

Geomechanical experiments on core samples from different parts of the reservoir complex were performed to determine elastic stiffness parameters and plastic strengths in various stress geometries. Cross plot of measured porosity and permeability were for the different core samples is displayed in Figure 13. The experimental descriptions is described in Appendices A and A.1. The whole database was shared in [22], while the impact of cooling and re-pressurization on effective stress, when compared to the plastic strength, was used to constrain the safe operation envelope during CO_2 injection [23]. Here, the envelope accounting for cooling and re-pressurization was assembled.

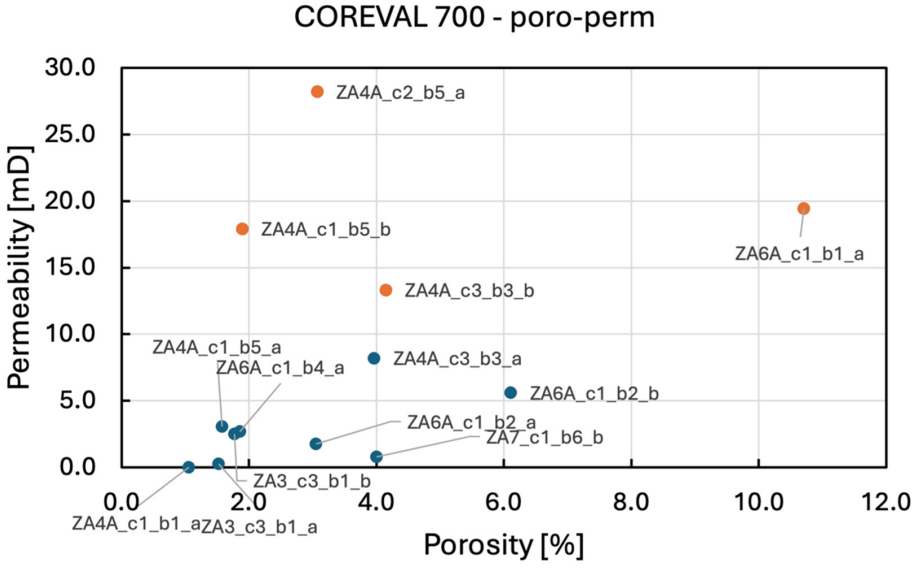

Figure 13. Porosity and permeability for the reservoir samples tested in the COREVAL 700 tool. Four highly permeable samples are used to determine the transmissibility multiplier.

In this paper, data from the COREVAL 700 tool were used to determine how pore volume and permeability are affected by hydrostatic confining stress changes. This was performed to estimate how porosity and permeability would change in respect to pore pressure by using the Biot effective stress concept. See Appendix A.1 for a description.

The results of all 14 reservoir samples are shown in Figure 14a, for volumetric strain, and Figure 14b, for rescaled permeability. A large variation between samples can be seen, which is linked to the large geological variability in-between samples, as displayed in Figure 13. With more than an order of magnitude differences in the permeability between the reservoir samples, the relation to confining stress becomes clear when the permeability is rescaled by the permeability at the initial measurement of 21 bar (Figure 14b). When calculating pore volume (porosity) and transmissibility (permeability) multipliers for the whole field (Figure 15), only selected high-porosity high-permeability samples with non-zero pore volume compressibility were used. These are marked with dashed lines in Figure 14a,b.

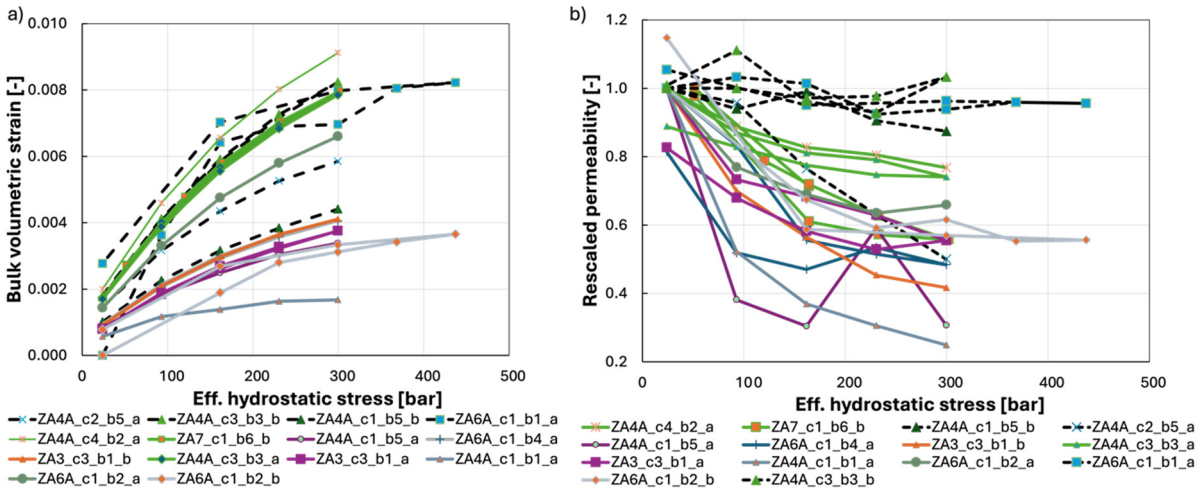

Figure 14. Bulk volumetric strain (**a**,**b**) permeability rescaled by the measured value at 21 bars as a function of Biot effective hydrostatic stress. For each curve, the well name, core and box number, and porosity and permeability in an unrested state are shown. Only reservoir samples are displayed here.

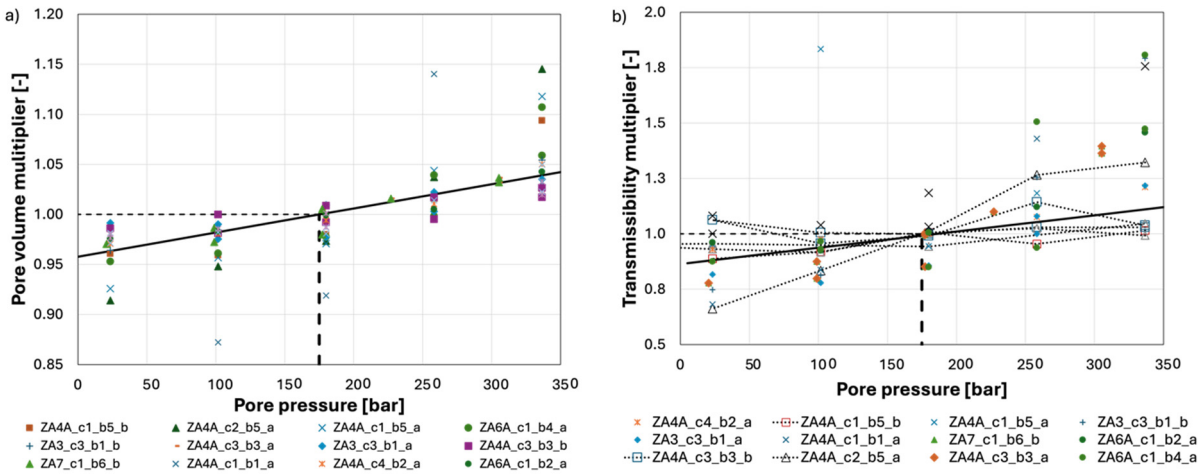

Figure 15. Pore volume (porosity) (**a**) and transmissibility (permeability) (**b**) multipliers displaying the relation between pore volume, permeability, and of pore pressure. The average relation from selected samples is shown as a solid line.

The analysis is valid in the elastic domain, as the applicability of the effective stress relation is limited to reversible deformation. These data are integrated into the reservoir simulations to mimic how porosity and permeability change dynamically during the injection of CO_2.

Because of the Biot effective stress principle, it is equivalent to vary pore pressure and the external confining stress in the elastic domain. Given the coordinate shift, as described in Appendix A.1, the estimated values were divided by the pore volume and permeability at a pressure of 175 bar so the pore volume and transmissibility multipliers were plotted (Figure 15a and Figure 15b, respectively). A large spread may be observed. The average response of the selected samples (dashed lines in Figure 14a,b) is expressed as solid black lines in Figure 15a,b. It is assumed that these rock samples are more relevant to mimic reservoir behavior, dominated by fracture-, not matrix-, driven flow mechanics.

The geomechanical strength of reservoir samples was determined in the tensile regime by Brazilian tests, in the shear strength by unconfined compressive strength and triaxial tests [22], and the stressstate at which pre-existing fractures occur is shown in *qp*-space in Figure 16. Given the uncertainty of stress, Biot coefficient, thermal–elastic coupling coefficient, and pore pressure, the initial stresses and the shifted stress configuration are displayed as green and gray areas in Figure 16 using Monte Carlo techniques [23]. This enables the calculation of the pore pressure and reservoir temperature at which 1% of the simulated cases were geomechanically unstable (Figure 17). This figure show at which pressure pre-existing fractures may re-open, and when new tensile fractures and shear failure may form as function of temperature.

As the COREVAL 700 tool shows a physical relation between pore pressure, pore volume, and permeability, this is only valid in the elastic regime. When the pore pressure exceeds the lowest horizontal tectonic stress (224 bars), pre-existing fractures re-open. This leads to an increase in the permeability, as displayed in Figure 18. Here, the estimated permeability and porosity multiplier are plotted, while the permeability multiplier is calculated as an exponential function of pressure as the fracture widths increase. If pore pressure further exceeds the least tectonic stress plus the tensile strength (267 bars), new fractures will develop. This was however not accounted for in the multipliers in Figure 18, since the maximum injection pressure in the pilot injection scenario was limited by the induced fracture pressure (267 bars).

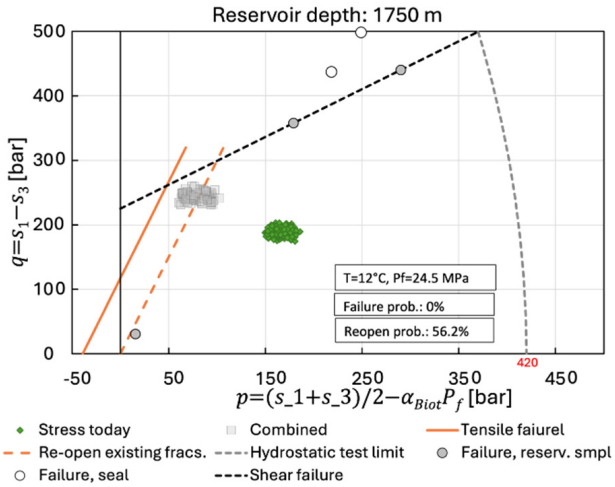

Figure 16. The reservoir strength envelope and reservoir effective stress (dots) at in situ conditions (52 °C and 172 bar in green) and in cooled and re-pressured states (12 °C and 240 bar (gray)). Variations in Earth stresses, thermal–elastic coupling coefficient, and Biot coefficient were used to span a likely range. The number of stress instances exceeding re-opening existing fractures, tensile failure, and shear failure is calculated for each pressure and temperature value. For more information [22,23].

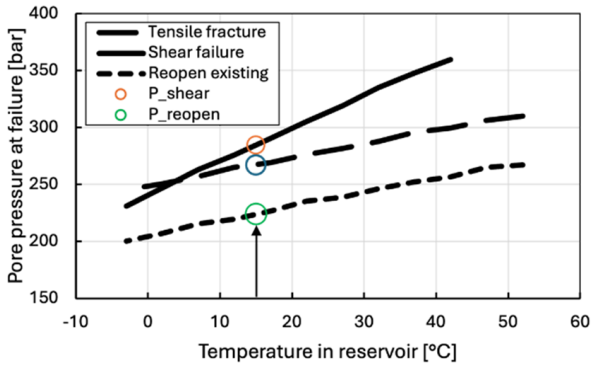

Figure 17. The pore pressure at which 1% of the Monte Carlo simulations induce failure for three failure modes as function of temperature. At 15 °C, the critical pore pressures were 224, 267, and 285 bars to re-open pre-existing fractures, to form new tensile fractures and shear failure, respectively. These critical pressures were used for the dynamic permeability exceeding the elastic limit (transmissibility multiplier).

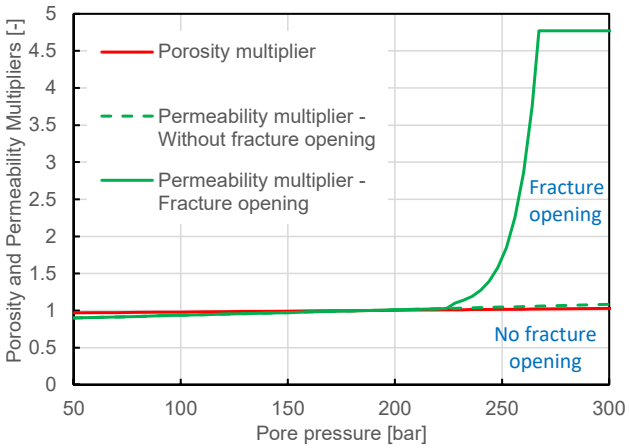

Figure 18. Porosity and permeability (without fracture opening) multipliers for the elastic regime (from Figure 15). As the pore pressure exceeds the threshold, as shown in Figure 17, the permeability multiplier for re-opening existing fractures (titled as fracture opening) is included.

The critical pressures above rely on the certainty of the input geomechanical data (i.e., the actual value and likely range), the risk of the operator reflected in the probability of failure (here 1%), and temperature.

3.4. Compositional Effects

A new compositional model was created for the history matching and prediction periods. The PVT data available provide a standard set of PVT experiments for the oil reservoir conducted at reservoir (52 °C) and close to standard (19 °C) conditions; however, this does not address the potential CO_2 interaction with reservoir fluids, as it was not relevant at the time of study. The Soave–Redlich–Kwong (SRK) equation of state was tuned to available data and both black-oil and eight-component compositional models were created. The models showed good matches for relative volumes, densities, and viscosities with a deviation within several percent.

Different correlations were used at reservoir temperature, including uncertainty to reservoir fluid parameters, to estimate the compositional interaction between CO_2 and reservoir fluids (Table 1).

Judging the correlation results, the minimum miscibility pressure is in the range of 153–182 bar, which is within the reservoir pressure range. A detailed CO_2 PVT study will be needed if this reservoir will be considered for CO_2-EOR, which can become an efficient

oil recovery technique. For the current study, where the model is used for evaluating the pilot injection into the aquifer zone, the MMP between the CO_2 and reservoir oil was set at 165 bars at 52 °C.

Table 1. Correlations used to model the interaction between CO_2 and reservoir fluids.

Temperature Current	Oil Density	Molecular Weight of C5+ [24], MW1	Molecular Weight of C5+ [25], MW2	MMP [26] for MW1	MMP [26] for MW2
°C	kg/m^3			bar	bar
52	903.2	252.4	256.7	152.7	155.7
52	911	294.0		181.6	

For the sake of reducing the simulation time in the current study, as, again, only the pilot CCS scenarios are to be simulated, the black-oil model representing CO_2 through the solvent option is used.

3.5. Geochemistry Effects

As CO_2 is injected into reservoirs, the near-well region is exposed to proportionally huge volumes of CO_2. It is then important to determine that the risk of formation damage is low, e.g., by salt precipitation, hydrate formation, fines migration, bacteria activity, and temperature and pressure cycling [27–29].

Among the geochemical effects, two may have a strong impact on the pilot CO_2 injection:

- Hydrate formation.
- Salt precipitation due to water drying out.

Hydrates form in higher pressure, lower temperature, and lower salinity environments. For the 180–200 bar system (high pressure in the vicinity of the injection well) of relatively low salinity, a CO_2 bottom hole temperature of at least 15 degrees should prevent hydrate formation. The expected low-rate injection in the pilot phase and geothermal heating as it travels down the well seem to provide a safe operational regime. Hydrate precipitation is therefore considered as a very low, easy to mitigate risk and will not be a part of the reservoir simulation study.

Potential salt precipitation seems to be the major risk factor for well injectivity during the pilot CO_2 injection. The injection of the dry CO_2 phase will evaporate water in water-bearing formations [30]. The concentration of ions in the water phase may then gradually increase until maximum solubility is reached, and salt precipitation may then occur. The potential of salt precipitation depends on several parameters, e.g., water-phase composition, residual water saturation, flow rate, pressure, and temperature. The risk of permeability reduction by salt precipitation depends on the location of the precipitate in the pore space and thereby on rock properties, fluid compositions, and local flow regimes.

Formation damage by salt precipitation includes three main mechanisms: salt precipitation, migration of salt crystals, and accumulation of crystals at pore throats [31]. Salt precipitation has been reported to cause pressure build-up and loss of injectivity in CO_2 projects. Studies related to the Ketzin project have reported dry-out radii in the range of 3.8–13 m and maximum halite saturations in the range of 3–80% [32]. For the Snøhvit project, a dry-out radius of 0.7 m was estimated for one reservoir zone [33]. In some other CO_2 projects, salt precipitation has been found to completely block perforations and the near-well region, e.g., the Aquistore project [34]. In the literature, mainly experiments with permeability reductions have been reported (up to 83%), but also some experiments with increases in permeability [30].

The extension of the dry-out/salt precipitation zone depends on parameters such as brine compositions, rock properties, flow regimes, and time [30,35]. Cui, Hu, Ning, Jiang, and Wang [36] found the extension of the dry-out zone to be large in high-porosity

and -permeability formations with not much formation damage, but less extension in low-porosity and -permeability formations with larger formation damage. The dry-out zone can be tens of meters, as reported for CO_2 projects [32,33]. Hurter, Labregere, and Berge [37] reported for a rock of 200 mD a zone of 10 m in 2 years, and Pruess [38] found the zone to be a few meters for a rock of 33 mD.

A mechanistic simulation was carried out to study salt precipitation near the wellbore. The reservoir salinity was 12,200 mg/L with chloride, and around 26,000 mg/L if all ions are taken together. The near-wellbore reservoir simulation was used to estimate the scale of salt precipitation in this case (assuming 25% residual water saturation, 60 m pay depth, and 30 mD permeability). Maximum salt precipitation reached 10% in the cell containing the well itself. After approximately half a year of injection, the salt precipitation zone stabilized, affecting in total only around 0.6 m around the wellbore (Figure 19). This study in combination with the literature referenced above were used as references for suggesting salt precipitation potential for the field in focus. The ranges for potential permeability reduction and the size of the near-wellbore area affected by salt precipitation were then assessed as: 10–80% and 0.5–5 m, correspondingly. These ranges were further converted into well skin factors (Appendix A.2) and applied to the sensitivity studies of CO_2 injection scenarios.

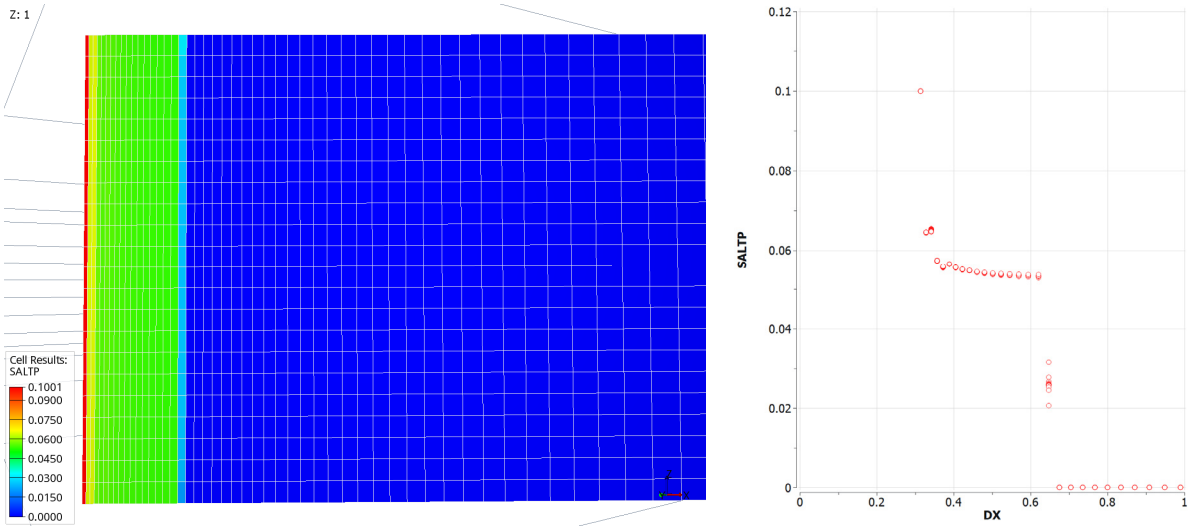

Figure 19. Salt precipitation in the near-wellbore area (full cross-section on the **left**) and concentration of precipitation salt vs. distance first meter from the well on the (**right**).

3.6. History Matching of the Reservoir Model

The geological model described in Section 3.1 was used as the basis for reservoir simulations. The model included the following reservoir properties: matrix porosity and permeability, as well as fracture intensity distributed on the fine geological grid with grid blocks of 10 × 10 × 1 m. These properties were redistributed on an upscaled grid (10 × 10 × 5 m) suitable for reservoir simulations in Eclipse software (version 2020.4) using the black-oil fluid flow model. Aiming at a further reduction of unneeded grid blocks laying in aquifer, out of the hydrocarbon-bearing area, a large part of the resulting aquifer grid-blocks was made inactive and replaced with the Fetkovich analytical aquifer model.

Based on the interpretation of the well, field, and experimental data available, the single-porosity and -permeability approach for reservoir flow simulations has been chosen. The choice was driven by the following arguments (following the studies summarized in the previous sections):

1. It was assumed that the pore volume was mainly constituted by pores and fracture-associated vugs.

2. Dual-porosity effects were not interpreted from the analysis of the pressure transient data available (dual-porosity signature in the pressure derivative) and production history (e.g., fast horizontal water breakthrough in the horizontal direction between the injection and production wells).
3. Effective permeability of the fractured reservoir was estimated from an analysis of the dynamic data available for many wells and distributed throughout the reservoir. The effective permeability estimated was much higher (50–1000 mD, resulting in the flow capacity in Figure 11) than the values obtained from the core measurements, 0.01–30 mD (Figure 13), which mainly represent the matrix permeability. In comparison to the core measurements, the dynamic data analysis represents reservoir-scale estimations (no need for upscaling from the lab-to-field level).
4. The fracture porosity estimation looks like an unattainable task, since the fracture description is limited by fracture density without a possibility to estimate fracture apertures and length.

Based on the arguments above, the series of fit-for-purpose reservoir simulations was carried out within the single-medium concept in the dynamic data analysis and evaluation of the salt precipitation effects described above. These simulations contributed to the full-field reservoir model update.

For the next step, the pore volume and transmissibility multipliers obtained from the geomechanical study described in Section 3.3 were specified. The resulting first version of the full-field model was then used to condition the matrix permeability distribution to the results of the dynamic data analysis summarized in Section 3.2. The matrix permeability resulting from geological modeling (Figure 20) was first conditioned to the fracture density distribution (Figure 8) and then to the permeability-thickness product obtained for different wells from the dynamic data analysis (Figure 11). The well-based multipliers were then inter- and extrapolated to the inter-well reservoir volumes using the moving average method available in Petrel.

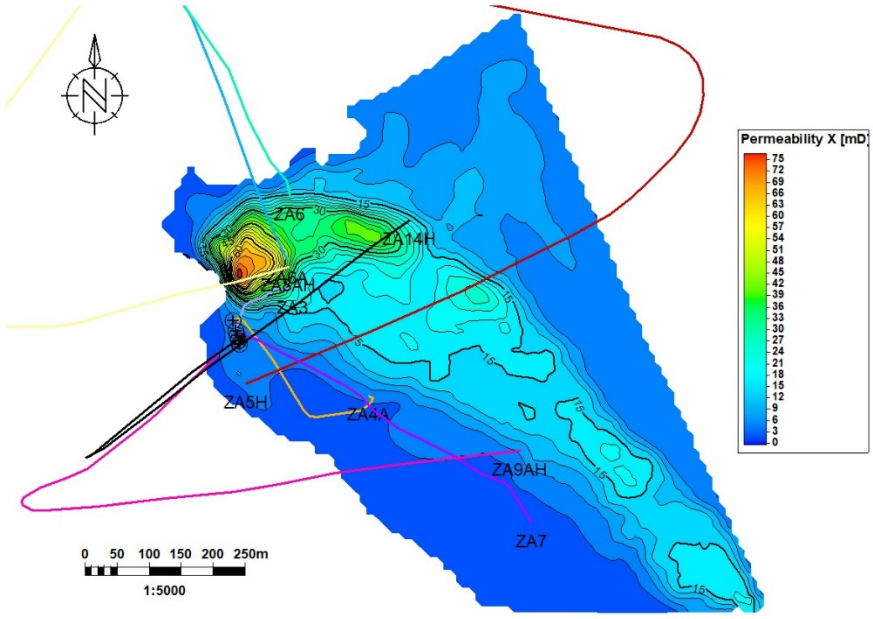

Figure 20. Map of thickness-averaged matrix permeability from the geological model.

The resulting permeability distribution was then tested in reproducing the field production history. It should be mentioned that implementing and distributing the well-based permeability multipliers obtained from the dynamic data analysis are tasks complicated by understanding which areas these values should be assigned to and how to inter- and extrapolate these multipliers in the inter-well area of the reservoir. Thus, the radius of investigation from the pressure transient analysis (PTA) was assigned to the multipliers

obtained for the wells in the dynamic data analysis. Additional spatial control of the multiplier distribution was applied to control the distribution in the inter-well area.

The updated permeability distribution obtained via conditioning of the permeability (initially conditioned to the fracture density) to the well-based multipliers was tested in history-matching exercises. Here, matching the well pressure history and well pressure drops were given the most attention. Further fine tuning of the multipliers for some wells was carried out to match the well measurements. As an example, the pressure history match for well ZA3 is shown in Figure 21. This fine tuning has provided some deviations of the resulting permeability-thickness product, if compared to the dynamic data analysis in Figure 11. At the same time, a reasonable match of the pressure history for all the wells has been achieved. For some wells, additional minor permeability adjustments were carried out to match the observed gas–oil ratios and water-cuts in individual producers. As a result of the conditioning of the permeability distribution to the dynamic data analysis results as well as matching to the production history, the final permeability map was created, as shown in Figure 22.

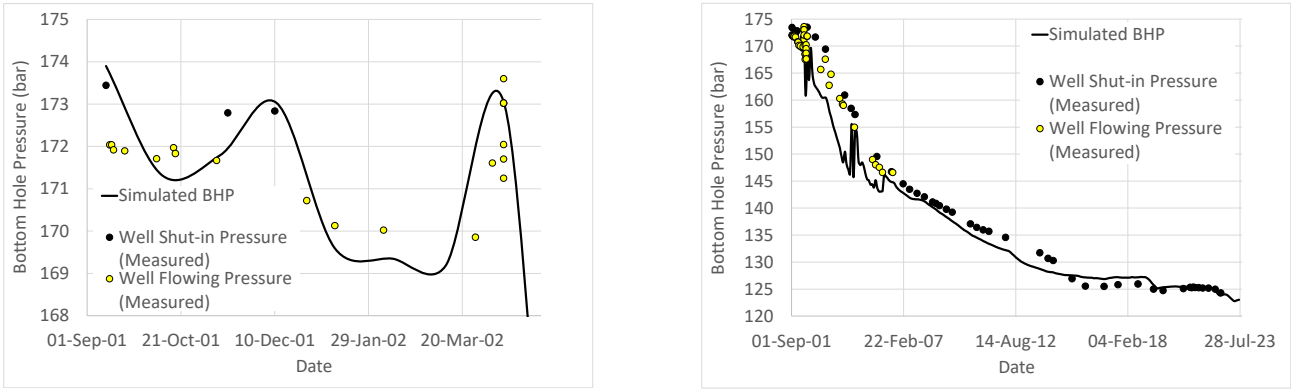

Figure 21. (**a**): Matching a period of pressure history of the ZA3 well. (**b**): Matching history of bottom hole pressure in the observation ZA3 well.

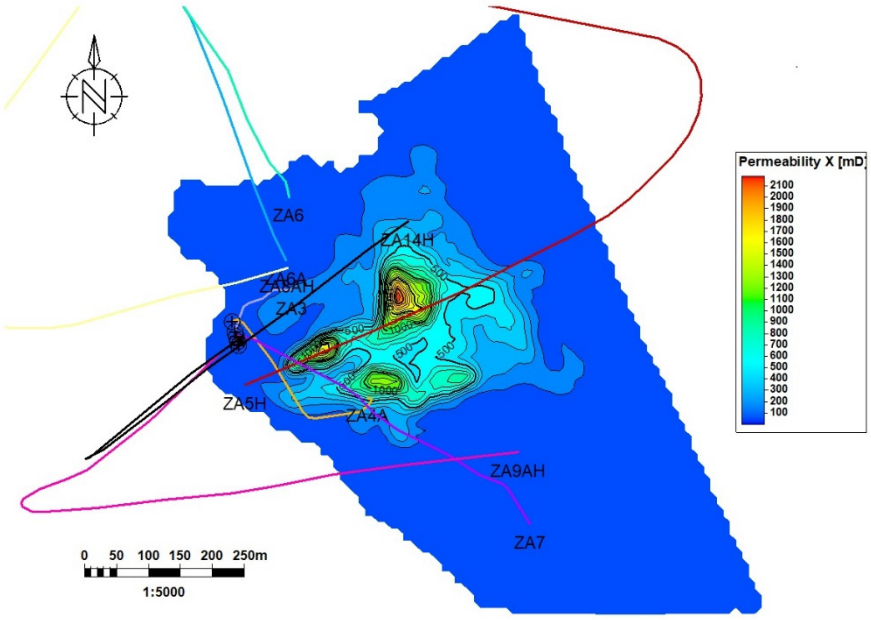

Figure 22. Map of thickness-averaged effective permeability of the fractured reservoir resulting from conditioning to dynamic data analysis results and history matching.

The results of the history matching of the full-field reservoir model may be illustrated with the history of the ZA3 well (the discovery and the first production well in the field). Having a long open-hole interval in the oil zone, the gas from the gas cap reached the top part of the open hole increasing the gas–oil ratio (GOR) to a level that caused the production from the well to be terminated. Since 2006, the producer was used as an observation well, allowing occasional (with retrievable gauges) measurements of the static bottom hole pressure (BHP). The pressure measurements were useful in the history-matching process allowing us to adjust initial hydrocarbon volumes and aquifer size and may also be used to evaluate the history-matching results. The comparison of the pressure measurements (circles) and the BHP simulation results (line) displayed in Figure 21 indicate a reasonable matching of the measurements by the simulation results. Achieving these history-matching results, the reservoir model was further used for the simulation of the pilot CO_2 injection scenarios.

3.7. Simulation of Pilot CO_2 Injection

The pilot CO_2 injection scenarios were set up taking into account the safe operating envelope resulting from the geomechanical evaluations described in Section 3.4. The highest-risk scenario of cold CO_2 injection at 15 °C was assumed, resulting in natural fracture opening at 224 bar and induced fracturing pressure at 267 bar (Figure 17), which was considered as the maximum injection BHP in the simulations. The impact of geochemical effects related to potential salt precipitation in the near-wellbore area was evaluated via sensitivity runs for the well skin factor following Table A1.

The solvent model, which is a four-component extension of the Eclipse black-oil model, was used to introduce CO_2 properties as the fourth reservoir fluid in addition to gas, oil, and water. The main scenario of the pilot CO_2 injection was considered with an injection into the ZA7 well, penetrating water zone. The pilot injection scenarios assumed the commencement of CO_2 injection without preceding gas cap depletion, where injection started during the current reservoir conditions. An alternative scenario of gas cap depletion following CO_2 injection may also be considered, but it is outside of the scope of this study.

The legislation of the Czech Republic allows for a cumulative injected volume at a maximum of 100 thousand tons of CO_2 for a pilot injection. Following this restriction, the pilot injection volumes were chosen as the mass injection rate of 44 thousand tons per year during nineteen months with 70 thousand tons injected in total.

One of the main advantages of commencing the CO_2 injection in the current reservoir conditions (before gas cap depletion) is that the reservoir pressure remains sufficiently high, avoiding the Joule–Thomson cooling effect observed during injections at low reservoir pressures. Another benefit here is CO_2 injected and flowing inside the reservoir in the supercritical phase.

The ZA7 well was chosen as the CO_2 injector profiting from the fact that the well is currently being used for water injection. The well was recently re-completed with fiberglass tubing, which makes it a perfect candidate for CO_2 injection, without significant additional costs for converting it into a CO_2 injector. The nearby ZA3 well is currently used as an observation well and therefore may be further used for reservoir monitoring during the pilot CO_2 injection. Well ZA7 penetrates the aquifer part of the field and CO_2 is therefore injected into the water zone.

Following the main CO_2 pilot injection design described above, the injection with a mass rate of 120 tons per day during the pilot injection period within 583 days (with 70 thousand tons cumulatively injected) was simulated. As the injection rate is relatively low, the calculated BHP in the injector increased during the pilot period only by 6 bars (from 137 to 143 bar), as can be observed in Figure 23a.

The corresponding increase in the average reservoir pressure is shown in Figure 23b in comparison to the pressure depletion from 174 to 121 bar during the production history. The simulation results predict a minor reservoir pressure increase of 9 bar (from 121 to 130 bar) during the pilot injection.

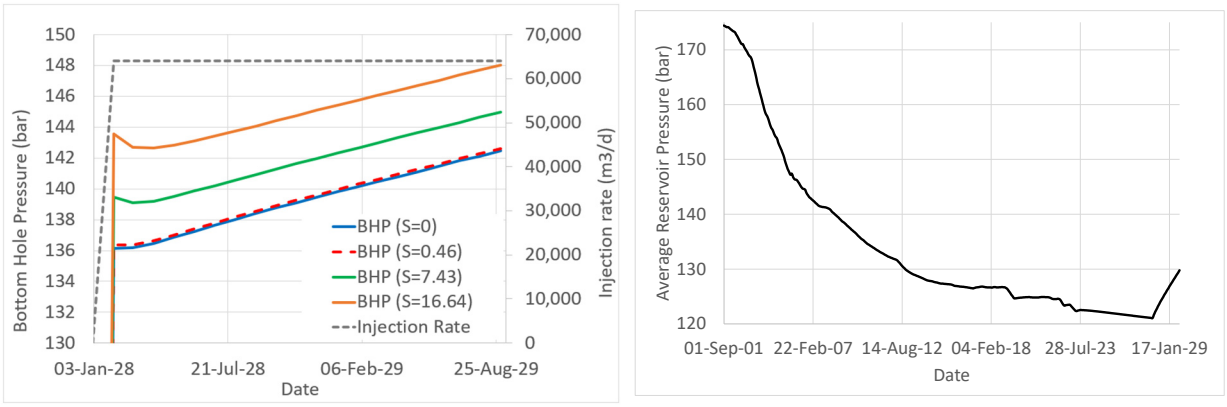

(**a**) (**b**)

Figure 23. (**a**): Simulated BHP for the pilot CO_2 injection into the ZA7 well; sensitivity to skin factor (S). (**b**): Average reservoir pressure during production history and the pilot CO_2 injection (base case with zero well skin).

The injected CO_2 has a lower density than formation water and oil, but higher than gas in the gas cap at the current reservoir pressure and temperature. Consequently, the injected CO_2 is first accumulated around the ZA7 injection well, forming a small CO_2 plume, starts to migrate throughout the formation structure (oil zone) and segregated by gravity at the top of the oil zone and bottom of the gas cap, as illustrated in Figure 24.

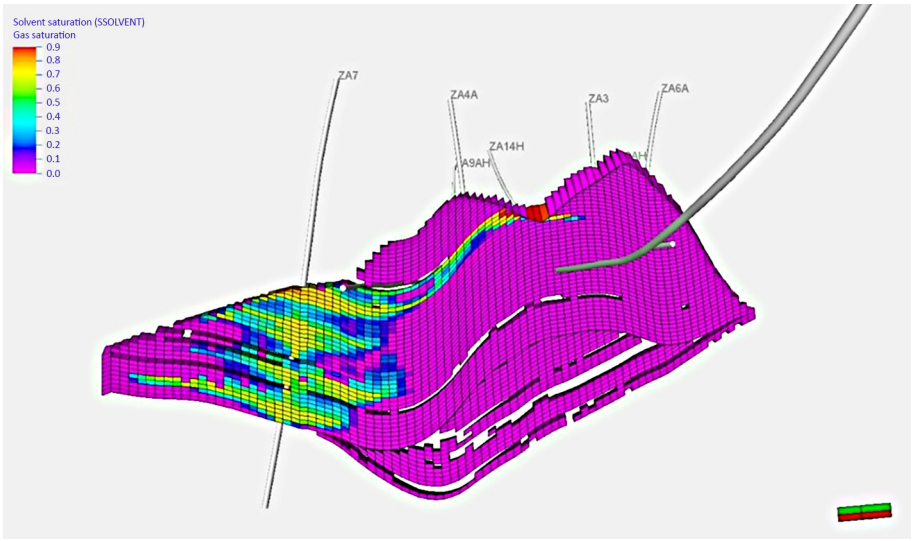

Figure 24. CO_2 saturation at the end of the pilot injection.

Additional simulations were carried out to quantify uncertainties associated with possible salt precipitation in the main pilot injection scenario. As discussed in Section 3.5, salt precipitation may cause permeability reduction in the near-wellbore area of a certain radius, which can be modeled by increasing the skin value in the injection well following Appendix A.2 in Appendix A. The sensitivity was assessed for the permeability, which reduced by 10 and 80%, and the radius of the near-wellbore area with the reduced permeability varying from 0.5 to 5 m. These ranges resulted in the skin values of 0.21 (10%, 0.5 m; this was ignored since is very close to zero), 0.46 (10%, 5 m), 7.43 (80%, 0.5 m), and 16.64 (80%, 5 m); see Appendix A.2. The pilot simulation described above assumed a zero skin value and was used as the reference case for skin sensitivity. The skin sensitivity of the pilot injection scenario is shown in Figure 23a, and demonstrates about 6 bar of additional pressure drop due to skin in the most risky scenario with a skin value of 16.64. So, the

presence of skin may double the BHP build-up during the pilot injection (achieving 148 bar), although the BHP remains far from the natural fracture opening pressure (224 bar).

As a final step, the potential CO_2 injection capacity of the reservoir assuming an injection at the maximum pressure of 267 bar corresponding to the induced fracturing pressure following the geomechanical evaluations for the temperature of 15 °C (Figure 17) was estimated. Here, since the well BHP may overcome the fracture opening pressure of 224 bar, the effect of fracture opening was also studied by applying two permeability multipliers: accounting and not accounting for the fracture opening (Figure 18). In addition, the well skin sensitivity (due to salt precipitation) was studied similarly to the simulations of the pilot injection above.

The simulation results in Figure 25a show that the CO_2 injection rate is significantly higher for the cases of low or no skin (0 and 0.46), since the reservoir pressure in the near-wellbore area is close to BHP (267 bar), which is much higher than the fracture opening pressure. This causes high pressure in the near-wellbore area and opening natural fractures. In the cases with high skin (7.43 and 16.64), a high well-reservoir pressure drop is established with the pressure in the near-wellbore area with exceeding the fracture opening pressure, only after some period of time (about half a year after the start of the injection for the case of a skin value of 7.43). This is an interesting interplaying effect between fracture opening and skin effects that should be accounted for in further evaluations of large-scale injection scenarios. The average reservoir pressure dynamics for the sensitivity runs are illustrated in Figure 25b. The total CO_2 storage capacity in all the scenarios with injection at induced fracturing pressures may be estimated as around 500 million m^3 or around 900 thousand tons (Figure 25c).

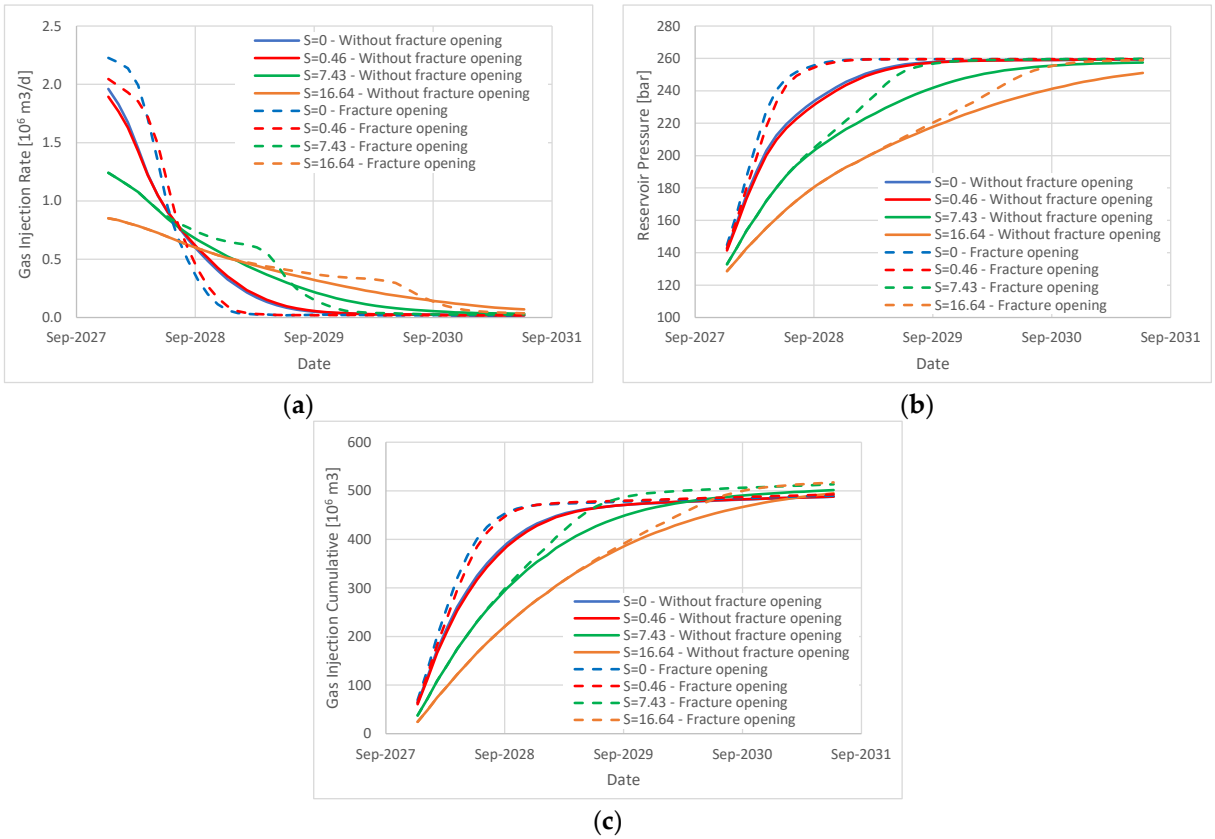

Figure 25. Sensitivity to salt precipitation and fracture opening in the scenario of CO_2 injection at maximum pressure: (**a**): CO_2 injection rate, (**b**): average reservoir pressure, and (**c**): gas injection cumulative volume.

4. Discussion

In this section, we discuss the uncertainties related to the integrated approach in the context of application to the site in focus, accounting for the field and experimental data available for the study.

4.1. Validity of Pressure-Dependent Multipliers Estimated from Geomechanical Analysis

Because of the validity of the Biot effective stress principle used in the geomechanical evaluations, obtained permeability and porosity multipliers are only limited by the elastic domain without any irreversible deformation occurring, such as fracturing. As is described in [23], the re-opening of existing fractures may start at a pore pressure of 220–250 bars. In this case, the effective reservoir permeability will increase significantly more than what is obtained here. As such, since the reservoir fluid flow is primarily focused on fractured rocks, the use of the geomechanical experiments shall be used with care.

There are, however, primarily two arguments that may be presented to still choose to use the data. First, it is the only direct datum that exists from the field, as field data analysis was carried out only for pressure depletion (not build-up) and did reveal permeability changes. In addition, microfractures are likely to exist at scales less than those observed for each sample, especially for the four samples with a low/moderate porosity and, relatively speaking, high permeability (see Figure 13). Here, it is likely that microfracture flow processes contribute to the observed permeability in the COREVEAL 700 tests.

Due to survival bias in the rock sample selection, it is likely that the rock mechanical tests display a too-high stiffness and strength compared to what would be the case for the reservoir scale. During drilling, coring, exhumation, storage, and handling only, the relatively stronger rock volumes with a size larger than, e.g., 5–10 cm, can be used for mechanical strength tests. This highlights the issue of lab-to-field upscaling in obtaining proper geomechanics descriptions for fractured rocks [23] to be addressed in further studies.

4.2. Uncertainty of the Safe Injection Envelope and Impact of CO_2 on Geomechanical Parameters

The safe injection envelope presented in Figure 17 is a result of the evaluation of the in-situ stress state and geomechanical experiments on intact rock samples [22], with following the application of Monte-Carlo modeling accounting for the uncertainty of the results of the experiments [23]. In the evaluation of the in-situ stresses, only limited data for other formations and other reservoir depths were used, since no in-situ stress estimates are available for the formation in focus. Geomechanical experiments were carried out on core samples with no or a very limited presence of natural fractures, since most of the fractured cores were disintegrated during the coring process. The impacts of the natural fractures on the geomechanical parameters evaluated and lab-to-field upscaling of the geomechanical effects for the fractured rocks were not accounted for in the Monte-Carlo modeling providing, as a result, the safe injection envelope. In combination with the uncertainty of the geomechanics experiments discussed above, the envelope assembled may also be uncertain. In particular, the presence of natural fractures may narrow down the envelope as described in [23].

It has previously been shown that the weak acid formed by CO_2 and brine mixtures might lead to carbonate dissolution that, in turn, has shown to modify rock strength (e.g., [39]. Nermoen, Porzer, Klempa, and Sancer [22] performed ultrasonic velocity measurements on three reservoir rock samples exposed to CO_2 and brine at in-situ conditions in batch experiments over three months. All three samples displayed a reduction in ultrasonic velocities and, thus, dynamic Young's modulus. As the dynamic stiffness was shown to correlate to strength, it could be expected that the rock mechanical strength also becomes affected by injected CO_2. Since the number of samples was low, and the impact was highly variable, it was concluded that firm conclusions on chemically induced mechanical weakening could not be drawn. Since tests were performed on intact rock samples, and the applicability to mechanical integrity of fractured carbonate is uncertain, this effect on the safe operation envelope was not included in the evaluation [23].

Further field studies and laboratory and well tests are therefore suggested to ensure a reliable evaluation of the safe injection envelope.

4.3. Approach to Reservoir Simulations of the Naturally Fractured Reservoir

The study of the fractured rocks resulted in matrix porosity (estimated from well logging data) and effective reservoir permeability (estimated from dynamic data analysis). Uncertainty of reservoir porosity also exists since fracture porosity was neglected in the study due to the reasons mentioned above. The matrix permeability estimated in the core experiments is in the range of 0.01–30 mD (Figure 13), while the dynamic data analysis of the effective reservoir permeability provided the range of 50–1000 mD, resulting in the estimated flow capacity shown in Figure 11. Any estimates for the fracture porosity were not obtained due to an inability to characterize the fracture apertures and fracture geometry from the available data, which is commonly a challenging task. As a result, the single-porosity model was employed to simulate flow in the reservoir, where the matrix porosity was used as the effective reservoir porosity, while the fracture permeability was used as the effective reservoir permeability. Such an approach looks like a reasonable option for the project's objectives and the effective permeability estimation seems to be quite certain, since it was obtained from flow data analysis and history matching. An uncertainty of the permeability estimation may be associated with describing the impact of the fracture geometry on distributing fractured areas and the permeability tensor. Here, characterizing the natural fracture networks in terms of fracture lengths and orientations would govern distributing the fracture properties in the inter-well area. At the same time, the production history did not show any indications of large permeability anisotropy, for example water breakthrough horizontally between the injection and nearby production wells.

Well interference and tracer injection and interpretations may help in improving the fracture description, although it may be costly and late considering the phase of the production and costs involved. As an option, the monitoring of pressure in nearby wells (with gauges installed below the GOC) during the test of pilot CO_2 injection may be suggested, providing a possibility to study inter-well communication and therefore provide information for improved fracture description and effective permeability anisotropy.

4.4. Compositional and Geochemistry Effects

As both the pilot and full field implementation focus solely on CO_2 storage, the compositional effects are less vital than for the enhanced hydrocarbon recovery process. The key elements will be the effect of impurities on CO_2 properties in the reservoir, freezing point, and hydrate formation. It may be advised to include measurements of the relative permeabilities and capillary pressures during the pilot phase to better predict CO_2 migration in the reservoir. Salt precipitation studies have been initiated and hydrate precipitation would also need to be looked at. Overall, pre-heating CO_2 on the surface will efficiently reduce a risk of hydrate formation and the preliminary simulation studies carried out to date indicate that drying out and salt precipitation should not become the showstoppers.

5. Conclusions

An integrated approach to reservoir simulations has been developed and tested for evaluating pilot CO_2 injection in a depleted, naturally fractured oil field on-shore Europe. The approach includes a few components combining a standard reservoir simulation workflow with specific components related to modeling naturally fractured reservoirs and CO_2 injection.

Special attention in the paper was paid to:

1. Characterizing and modeling of fracture impact, including fracture analysis from well data and the evaluation of effective flow properties of the fractured reservoir from dynamic field data analysis.
2. Geomechanical assessments contributing to (i) assembling, history matching, and forecasting CO_2 injection using the reservoir model via applying pressure-sensitive

reservoir properties in the reservoir simulations, as well as (ii) assembling a safe injection envelope for conditioning CO_2 injection scenarios.

3. Accounting for compositional and potential geochemistry effects (salt precipitation) on CO_2 injection simulations and the performance of the CO_2 injection scenarios.

The application of the integrated approach to the depleted oil field allowed for evaluating pilot CO_2 injection scenarios and confirmed the reservoir capacity, above the planned pilot injection volumes. The simulation study has also provided CO_2 migration pathways driven by gravity. Based on the simulations, injected CO_2 into water zone should migrate upward and accumulate below the remaining gas in the gas cap and above the remaining oil and water.

The application of the approach to the site in focus has also revealed large uncertainties, related to fracture description and geomechanical evaluations, resulting in an uncertain safe injection envelope [23]. These uncertainties are related to (1) limited knowledge of the in situ stress state without any stress estimates available for the site in focus [22]; (2) accounting for fracture impacts in the geomechanical evaluations of the fractured rocks; and (3) lab-to-field upscaling of the results of the geomechanical experiments [23]. The study by Nermoen, Shchipanov, Porzer, and Sancer [23] has indicated that the presence of natural fractures may have a strong impact on the geomechanical parameters of fractured rocks. Any chemo-mechanical effects on rock strength are not indicated in the geomechanical parameters obtained, but more work is needed to quantify its effect on fractured carbonates.

Thus, as more information is gathered, there is a potential of narrowing the safe injection envelope that may reduce the maximum injection pressure to avoid induced fracturing, and therefore, reduce the injection capacity of the site in focus. Additional field studies, including well tests, and laboratory experiments with further geomechanical modeling were suggested to reduce these uncertainties and verify the safe injection envelope [23].

Author Contributions: M.P.: reservoir simulations, and paper writing and editing; V.O.: geological modeling and paper writing; A.S.: integrated approach, dynamic data analysis, and paper writing and editing; A.N.: geomechanics, and paper writing and editing; R.B.: compositional effects and geochemistry, and paper writing and editing; I.F.: geochemistry and paper writing; J.R.: fracture characterization and modeling. All authors have read and agreed to the published version of the manuscript.

Funding: The CO_2-SPICER project is funded by EEA and Norway grants and by grant of the Technology Agency of the Czech Republic (grant number TO01000112).

Data Availability Statement: The field data used in this paper are owned by the field operator (MND); permission from MND is therefore required for sharing any part of the data.

Acknowledgments: The approach presented in this paper has been developed and applied within the CO_2-SPICER project and our colleagues participating in the project from the collaborative institutions, Norwegian Research Centre (NORCE), Czech Geological Survey (CGS), and Technical University of Ostrava (VSB), as well as the industry partner, MND, are gratefully acknowledged for their help and discussions, which facilitated the approach development and application. MND is acknowledged for permission to publish this paper.

Conflicts of Interest: Author Milan Pagáč and Vladimír Opletal were employed by the Moravské Naftové Doly (MND). The remaining authors declare that the research was conducted in the absence of any commercial or financial relationships that could be construed as a potential conflict of interest.

Abbreviations

3D	three-dimensional
BHP	bottom hole pressure [bar]
CCS	carbon capture and storage
CGS	Czech Geological Survey
CO_2	carbon dioxide
DDA	dynamic data analysis

FMS	formation microscanner
GOC	gas–oil contact
GOR	gas–oil ratio
GPa	giga pascal
mD	milli Darcy
MD	measured depth [m]
MND	Moravské naftové doly
MW	molecular weight
NMR	nuclear magnetic resonance
NORCE	Norwegian Research Centre
NW	North-West
OWC	oil–water contact
PDG	permanent downhole gauges
PTA	pressure transient analysis
PVT	pressure–volume–temperature
S	skin [-]
SCAL	special core analysis
SE	South-East
SRK	Soave–Redlich–Kwong

Appendix A

Appendix A.1. Geomechanical Experiments and Analysis

Cores from the MND repository were drilled with 37 mm diameter and varying lengths before polishing. Samples used in hydrostatic loading experiments was mounted in the COREVAL 700 tool where pore pressure was increased to 20 bar, and kept constant through the test, while the hydrostatic stress was simultaneously increased to 41 bar and then loaded by 69 bar steps to 317 and 455 bar. For each hydrostatic stress (σ_p), pore volume (V_p) and permeability were obtained using a stepwise injection of nitrogen (N_2) while monitoring the pore pressure response. Given the known PVT-behaviour of N_2, the pore volume of the specimen was determined. Moreover, from the pressure equilibration time, the permeability (k) was estimated.

The equivalence between hydrostatic stress and pore pressure variation is described by the effective stress relation from the external hydrostatic stress minus Biot coefficient multiplied by pore pressure:

$$\sigma' = \sigma_p - \alpha P_f \tag{A1}$$

Given a constant pore pressure of 20 bar, and Biot coefficient of 0.88 [22], the hydrostatic effective stress was varied. In 12 tests the effective stress varied from 21 to 297 bar, while 2 tests were loaded till 435 bar. 7 of the samples were exposed to a loading only, while 7 samples were both loaded and un-loaded.

For each step in effective stress, the pore volume and nitrogen permeability were measured, enabling $V_p(\sigma')$ and $k(\sigma')$. Given that calcium carbonate is the primary constituency with a mineral stiffness of $K_s = 74$ GPa the solid volume evolution is estimated via $V_s(\sigma') = V_{s,0}\ (1 - K_s\sigma')$, where V_{s0} was the solid volume in the 21 bar effective stress state as estimated via $V_{s,0} = (1 - \phi)V_{b,0}$, where ϕ was the porosity and $V_{b,0}$ the initial bulk volume. From the solid volume and measured pore volume, the bulk volume for each effective stress was determined via $V_b(\sigma') = V_s(\sigma') + V_p(\sigma')$. As such, the bulk volumetric strain was estimated via $\varepsilon_{vol} = -(V_b - V_{b,0})/V_{b,0}$ so volumetric strain as function of confining stress for all 14 samples could be displayed in Figure 14a (see also Nermoen 2024a for how bulk modulus relate to porosity).

The Eclipse simulations allow for porosity and permeability changes in response to pore pressure variations. In the COREVAL 700 tests, the external stress was changed, while by re-organizing Equation (A1) with respect to pore pressure, a co-ordinate shift was used to determine how the observed pore volumes and permeabilities related to porosity:

$$P_f = \frac{\overline{\sigma} - \sigma'_p}{\alpha} = \frac{350 - \sigma'_p}{0.88} \quad \text{(A2)}$$

where $\overline{\sigma} = \frac{\sigma_1+\sigma_3}{2} = 350$ bar was used from estimates of vertical weight (410 bar) and least horizontal stress (230 bar) from uniaxial strain assumption and Poisson ratio [23]. Now, for each value of pore pressure the pore volume and permeability were obtained, i.e., $V_p(P_f)$ and $k(P_f)$, was obtained from the measurements.

In the reservoir the initial hydrostatic pore pressure at 1750 m depth was 175 bar, and the pore volume and permeability at this pore pressure was then used as a reference for scaling, i.e., $V_p(175\,\text{bar}) = V_{p,ref}$ and $k(175\,\text{bar}) = k_{ref}$. This number was used to scale changes in porosity and permeability as function of pore pressure, as relative changes are more appropriate due to the large geological variability between samples. Based on this, the pore volume and transmissibility multiplier, could be determined via:

$$T_{pore} = \frac{V_p(P_f)}{V_{p,ref}} \quad \text{(A3)}$$

$$T_{perm} = \frac{k(P_f)}{k_{ref}} \quad \text{(A4)}$$

Appendix A.2. Well Skin to Approximate Salt Precipitation Effect

The salt precipitation effect in the near wellbore area of the reservoir may be approximately modelled using the well skin factor concept [21]. The skin may be calculated based on permeability reduction inside a limited near wellbore area as [21]:

$$S = \left(\frac{k}{k_S} - 1\right) ln \frac{r_S}{r_w} \quad \text{(A5)}$$

where S is well skin, dimensionless; k–reservoir permeability, mD; k_S–reduced permeability due to salt precipitation; r_S–radius of reduced permeability area, m; r_S–wellbore radius, m.

Based on the results of evaluations of potential salt precipitation effects discussed above, the following ranges for permeability reduction and damaged near wellbore area were suggested: 10–80% and 0.5–5 m. Following the Equation (A5), a set of well skin factors based on these ranges may be calculated as listed in Table A1. First three skin values were used in the sensitivity simulation runs focused on evaluating risks associated with salt precipitation for the CO_2 pilot injection performance.

Table A1. Permeability reduction ratio, radius of reduced permeability area and resulted skin factor calculated using the relationship (A5).

Permeability Reduction [Frac]	Damage Zone [m]	Well Skin [Dimensionless]
0.2	5	16.64
0.2	0.5	7.43
0.9	5	0.46
0.9	0.5	0.21

References

1. Barenblatt, G.; Zheltov, I.; Kochina, I. Basic Concepts in the Theory of Seepage of Homogeneous Liquids in Fissured Rocks. *J. Appl. Math. Mech.* **1960**, *24*, 852–864. [CrossRef]
2. Warren, J.; Root, P. The Behavior of Naturally Fractured Reservoirs (SPE-426-PA). *SPE J.* **1963**, *3*, 245–255. [CrossRef]
3. van Golf-Racht, T. *Fundamentals of Fractured Reservoir Engineering*; Elsevier: Amsterdam, The Netherlands, 1982.
4. Bourdet, D.; Ayoub, J.; Pirard, Y. Use of Pressure Derivative in Well-Test Interpretation (SPE-12777-PA). *SPE Form. Eval.* **1989**, *4*, 293–302. [CrossRef]

5. Bourbiaux, B.; Basquet, R.; Cacas, M.; Daniel, J.; Sarda, S. An Integrated Workflow to Account for Multi-Scale Fractures in Reservoir Simulation Models: Implementation and Benefits (SPE-78489). In Proceedings of the 10th Abu Dhabi International Petroleum Exhibition and Conference, Abu Dhabi, United Arab Emirates, 13–16 October 2002; SPE: Dubai, United Arab Emirates, 2002. [CrossRef]
6. Kuchuk, F.; Biryukov, D.; Fitzpatrick, T. Fractured Reservoir Modeling and Interpretation (SPE-176030-PA). *SPE J.* **2015**, *20*, 893–1004. [CrossRef]
7. Machado, V.; Delshad, M.; Sepehrnoori, K. Injectivity assessment for CCS field-scale projects with considerations of salt deposition, mineral dissolution, fines migration, hydrate formation, and non-Darcy flow. *Fuel* **2023**, *353*, 129148. [CrossRef]
8. Bohloli, B.; Skurtveit, E.; Grande, L.; Titlestad, G.; Børresen, M.; Johnsen, Ø.; Braathen, A. Evaluation of reservoir and cap-rock integrity for the Longyearbyen CO_2 storage pilot based on laboratory experiments and injection tests. *Nor. J. Geol.* **2014**, *94*, 171–187.
9. Fjær, E.; Holt, R.; Horsrud, P.; Raaen, A. *Petroleum Related Rock Mechanics*, 2nd ed.; Elsevier: Amsterdam, The Netherlands, 2008.
10. Bandis, S.C.; Lumsden, A.C.; Barton, N.R. Fundamentals of rock joint deformation. *Int. J. Rock Mech. Min. Sci. Geomech. Abstr.* **1983**, *20*, 249–268. [CrossRef]
11. Shchipanov, A.; Kollbotn, L.; Surguchev, L.; Thomas, K. A New Approach to Deformable Fractured Reservoir: Case Study of the Ekofisk Field (SPE 130425). In Proceedings of the SPE EUROPEC/EAGE Annual Conference and Exhibition, Barcelona, Spain, 14–17 June 2010; SPE: Barcelona, Spain, 2010. [CrossRef]
12. Shchipanov, A.; Kollbotn, L.; Prosvirnov, M. Step rate test as a way to understand well performance in fractured carbonates (SPE-185795). In Proceedings of the SPE Europec featured at 79th EAGE Annual Conference & Exhibition, Paris, France, 12–17 June 2017. [CrossRef]
13. Iding, M.; Ringrose, P. Evaluating the impact of fractures on the performance of the In Salah CO_2 storage site. *Int. J. Greenh. Gas Control* **2010**, *4*, 242–248. [CrossRef]
14. Ringrose, P.S.; Mathieson, A.S.; Wright, I.W.; Selama, F.; Hansen, O.; Bissell, R.; Saoula, N.; Midgley, J. The In Salah CO_2 Storage Project: Lessons Learned and Knowledge Transfer. *Energy Procedia* **2013**, *37*, 6226–6236. [CrossRef]
15. Bohloli, B.; Ringrose, P.; Grande, L.; Nazarian, B. Determination of the fracture pressure from CO_2 injection time-series datasets. *Int. J. Greenh. Gas Control* **2017**, *61*, 85–93. [CrossRef]
16. Berenblyum, R.; Khrulenko, A.; Kollbotn, L.; Nermoen, A.; Shchipanov, A.; Skadsem, H.J.; Zuta, J.; Hladik, V. Integrated Approach to CO_2 EOR and Storage Potential Evaluation in an Abandoned Oil Field in Czech Republic. In Proceedings of the 19th European Symposium on Improved Oil Recovery, Stavanger, Norway, 24–27 April 2017; EAGE: Stavanger, Norway, 2017. [CrossRef]
17. Hladik, V.; Opletal, V.; Berenblyum, R.; Porzer, M.; Prochac, R.; Jirman, P.; Shchipanov, A.; Nermoen, A.; Ford, E. Assessment of a mature hydrocarbon field in SE Czech Republic for a CO_2 storage pilot. In Proceedings of the 16th Greenhouse Gas Control Technologies Conference (GHGT-16), Lyon, France, 23–24 October 2022. [CrossRef]
18. Berenblyum, R. *ECO-BASE Establishing CO_2 Enhanced Oil Recovery Business Advantages in South Eastern Europe*; EERA Meeting: Brussel, Belgium, 2017.
19. Francu, J.; Ocásková, D.; Pařízek, P.; Vácha, J.; Pereszlényi, M.; Jirman, P.; Opletal, V.; Ličbinská, M. Geochemistry and Petrology of Reservoir and Cap Rocks in Zar-3 Pilot CO_2 Storage Complex, SE Czechia. *Geosciences* **2024**, *14*, 119. [CrossRef]
20. Shchipanov, A.; Berenblyum, R.; Kollbotn, L. Pressure Transient Analysis as an Element of Permanent Reservoir Monitoring (SPE-170740). In Proceedings of the SPE Annual Technical Conference and Exhibition, Amsterdam, The Netherlands, 27–29 October 2014. [CrossRef]
21. Bourdet, D. *Well Test Analysis: The Use of Advanced Interpretation Models*; Elsevier: Amsterdam, The Netherlands, 2002.
22. Nermoen, A.; Porzer, M.; Klempa, M.; Sancer, J. Geomechanical Data Base of Rock Samples from the Žarošice Hydrocarbon and Storage Complex (South Moravia, Czech Republic): Petrophysics, Stiffness, Strength, and Effective Stress Estimates for Mechanical Stability Evaluations during CO_2 Injection. 2024. Available online: https://zenodo.org/communities/co2spicer/records?q=&l=list&p=4&s=10&sort=newest (accessed on 22 May 2024).
23. Nermoen, A.; Shchipanov, A.; Porzer, M.; Sancer, J. Evaluation of safe operating envelope for CO_2 injection under uncertain rock mechanical parameters and earth stresses. *J. Greenh. Gas Control* **2024**. Available online: https://zenodo.org/communities/co2spicer/records?q=&l=list&p=1&s=10&sort=newest (accessed on 22 May 2024).
24. Lasater, J. Bubble point pressure correlation. *J. Pet. Technol. Soc. Pet. Eng.* **1958**, *10*, 65–67. [CrossRef]
25. Mungan, N. *Heavy Cruid Oil Recovery*; Chapter Carbon Dioxide Flooding-Fundamentals; Springer: Berlin/Heidelberg, Germany, 1981; Volume 20, p. 87. [CrossRef]
26. Holtz, M.; Lopez, V.; Breton, C. *Moving Permian Basin Technology to the Gulf Coast: The Geologic Distribution of CO_2 EOR Potential in Gulf Coast Reservoirs.* West Texas Geological Society Publication No. 05-115 Presented at the Fall Symposium, October 26–27. 2005. Available online: https://citeseerx.ist.psu.edu/document?repid=rep1&type=pdf&doi=613e955f194c9fa4bb2b3fe3ba9fd1b90ec5b9f3 (accessed on 5 March 2024).
27. Hansen, O.; Gilding, D.; Nazarian, B.; Osdal, B.; Ringrose, P.; Kristoffersen, J.B.; Eiken, O.; Hansen, H. Snøhvit: The History of Injecting and Storing 1 Mt CO_2 in the Fluvial Tubåen. *Energy Procedia* **2013**, *37*, 3565–3573. [CrossRef]
28. Sminchak, J.; Zeller, E.; Bhattacharya, I. Analysis of unusual scale build-up in a CO_2 injection well for a pilot-scale CO_2 storage demonstration project. *Greenh. Gases Sci. Technol.* **2014**, *4*, 357–366. [CrossRef]

29. Zettlitzer, M.; Moeller, F.; Morozova, D.; Lokay, P. Re-establishment of the proper injectivity of the CO_2-injection well Ktzi 201 in Ketzin, Germany. *Int. J. Greenh. Gas Control* **2010**, *4*, 952–959. [CrossRef]
30. Miri, R.; Hellevang, H. Salt precipitation during CO_2 storage—A review. *Int. J. Greenh. Gas Control* **2016**, *51*, 136–147. [CrossRef]
31. Ott, H.; Snippe, J.; de Kloe, K. Salt precipitation due to supercritical gas injection: II. Capillary transport in multi porosity rocks. *Int. J. Greenh. Gas Control* **2021**, *105*, 103233. [CrossRef]
32. Baumann, G.; Henninges, J.; Lucia, D. Monitoring of saturation changes and salt precipitation during CO_2 injection using pulsed neutron-gammalogging at the Ketzin pilot site. *Int. J. Greenh. Gas Control* **2014**, *28*, 134–146. [CrossRef]
33. Grude, S.; Landrø, M.; Dvorkin, J. Pressure effects caused by CO_2 injection in the Tubåen Fm., the Snøhvit field. *Int. J. Greenh. Gas Control* **2014**, *27*, 178–187. [CrossRef]
34. Talman, S.; Shokri, A.; Chalaturnyk, R.; Nickel, E. Chapter 11. Salt precipitation at an active CO_2 injection site. In *Gas Injection into Geological Formations and Related Topics*; Wu, A., Zhu, W., Carroll, J.J., Hao, M., Eds.; Wiley: Hoboken, NJ, USA, 2020. [CrossRef]
35. Afanasyev, A.; Grekho, S. Analytical expression for the skin factor of the salt deposition zone around a CO_2 injection well: Extension to the case of ternary miscible displacement. *Geoenergy Sci. Eng.* **2023**, *228*, 212036. [CrossRef]
36. Cui, G.; Hu, Z.; Ning, F.; Jiang, S.; Wang, R. A review of salt precipitation during CO_2 injection into saline aquifers and its potential impact on carbon sequestration projects in China. *Fuel* **2023**, *334*, 126615. [CrossRef]
37. Hurter, S.; Labregere, D.; Berge, J. Simulations for CO_2 injection projects with compositional simulator. In Proceedings of the SPE Offshore Europe Oil and Gas Conference and Exhibition, Aberdeen, UK, 4–7 September 2007; SPE 108540. SPE: Aberdeen, UK, 2007; pp. 1–7. [CrossRef]
38. Pruess, K.M. Formation dry-out from CO_2 injection into saline aquifers: 1. Effects of solids precipitation and their mitigation. *Water Resour. Res.* **2009**, *45*, 1–11. [CrossRef]
39. Nermoen, A.; Korsnes, R.; Hiorth, A.; Madland, M. Porosity and permeability development in compacting chalks during flooding of nonequilibrium brines: Insights from long-term experiment. *J. Geophys. Res. Solid Earth* **2015**, *120*, 2235–2960. [CrossRef]